

Rochester Institute of Technology

RIT Digital Institutional Repository

Theses

11-1-2010

Characterization of two-phase flow in a transparent PEM fuel cell using simultaneous anode and cathode visualization and digital image processing

Jacqueline Sergi

Follow this and additional works at: <https://repository.rit.edu/theses>

Recommended Citation

Sergi, Jacqueline, "Characterization of two-phase flow in a transparent PEM fuel cell using simultaneous anode and cathode visualization and digital image processing" (2010). Thesis. Rochester Institute of Technology. Accessed from

This Thesis is brought to you for free and open access by the RIT Libraries. For more information, please contact repository@rit.edu.

Characterization of Two-Phase Flow in a Transparent PEM Fuel Cell using Simultaneous Anode and Cathode Visualization and Digital Image Processing

by

Jacqueline M. Sergi

A Thesis Submitted in Partial Fulfillment of the Requirements for the Degree of

MASTER OF SCIENCE

in

MECHANICAL ENGINEERING

Approved by:

Dr. Satish G. Kandlikar

Department of Mechanical Engineering

(Thesis Advisor)

Dr. Steven W. Day

Department of Mechanical Engineering

Dr. Robert J. Stevens

Department of Mechanical Engineering

Dr. Wayne W. Walter

Department of Mechanical Engineering

(Department Representative)

DEPARTMENT OF MECHANICAL ENGINEERING
ROCHESTER INSTITUTE OF TECHNOLOGY
NOVEMBER 2010

Thesis Reproduction Permission Statement

Permission Granted

Title:

Characterization of Two-Phase Flow in a Transparent PEM Fuel Cell using Simultaneous Anode and Cathode Visualization and Digital Image Processing

I, *Jacqueline M. Sergi*, hereby grant permission to the Wallace Library of Rochester Institute of Technology to reproduce my thesis in whole or in part. Any reproduction will not be for commercial use or profit.

Date: _____ Signature of Author: _____

I. Abstract

Proton exchange membrane (PEM) fuel cells have emerged as a potential alternative to internal combustion engines in order to curb dependency on fossil fuels and reduce harmful CO₂ emissions. Water management has been identified as a key research area for the advancement of PEM fuel cell technology, especially as it affects the purge protocol prior to cell shutdown. The presence of water in the cell is necessary to sustain membrane hydration, but the accumulation of excess liquid water, referred to as flooding, can lead to increased mass transport losses and reductions in performance and durability. In this work, a technique was developed to characterize the two-phase flow in the anode and cathode flow field channels simultaneously using a transparent fuel cell with dual-visualization capability. The transparent fuel cell used in this work was designed to represent actual full scale automotive fuel cell geometry. A video processing algorithm was developed to automatically detect dynamic and static liquid water present in the gas channels and generate relevant quantitative information. The water coverage ratio is introduced as a parameter to capture the time-averaged flow field water content information through recorded video sequences. The algorithm also yields information pertaining to the distribution of water among different two-phase flow structures. The water coverage ratio and distribution metrics were employed in comparing the performance of Freudenberg and Toray gas diffusion layers (GDLs) from a water management perspective, including direct anode to cathode comparisons for each GDL sample. This technique was able to provide a unique and comprehensive characterization of liquid water in an operating fuel cell which can be used towards the optimization of water management and purge strategies, as well as data generation for model validation purposes.

II. Table of Contents

I. Abstract	iii
II. Table of Contents	iv
III. Index of Tables and Figures	vi
i. Figures	vi
ii. Tables	x
IV. Nomenclature	xi
1. Introduction	1
2. Literature Review	5
2.1. Summary of Research Needs	14
2.2. Scope of Work	15
3. Experimental Methodology	16
3.1. Overview of Experimental Work	16
3.2. Experimental Setup	16
3.2.1. System Overview	16
3.2.2. Transparent PEM Fuel Cell Design	17
3.2.3. Dual-Visualization Setup	20
3.2.4. Material Properties of Cell Components	22
3.3. Experimental Procedure	23
3.3.1. Fuel Cell Operating Conditions	23
3.3.2. Fuel Cell Testing Procedure	24
3.3.3. Data Acquisition and Processing	25
3.3.4. Video Recording Procedure	25
4. Digital Video Processing Methodology	27
4.1. Overview	27
4.2. Analysis of Digital Videos and Images	27
4.3. Theory of Morphological Image Processing	29
4.4. Video Processing Algorithm	33
4.4.1. Input Files	33
4.4.2. Pre-Processing	34
4.4.3. Image Subtraction and Segmentation	35

4.4.4. Application of Morphological Image Processing.....	39
4.5. Calculation of Relevant Metrics	44
4.6. Slug and Film Detection using Connected Components	44
5. Results and Discussion.....	48
5.1. Fuel Cell Performance Characterization.....	48
5.2. Visual Observations of Two-Phase Flow in the Gas Channels	50
5.2.1. Stoichiometric Ratio 1.5/2.5.....	50
5.2.2. Stoichiometric Ratio 1.5/5.....	53
5.2.3. Stoichiometric Ratio 3/8.....	54
5.3. Automatic Detection of Static and Dynamic Liquid Water.....	55
5.4. Water Coverage Ratio.....	59
5.4.1. Stoichiometric Ratio 1.5/2.5.....	59
5.4.2. Stoichiometric Ratio 1.5/5.....	60
5.4.3. Stoichiometric Ratio 3/8.....	61
5.4.4. Tabulated Water Coverage Ratio Results	62
5.5. Flow Structure Differentiation and Water Distribution	63
5.5.1. Tabulated Water Distribution Results	66
5.6. Summary of Experimental Results	67
6. Conclusions	68
7. Recommendations for Future Work	70
8. References	71
9. Appendices	74
9.1. Appendix A: Water Detection and Quantification Algorithm (MATLAB)	74
9.2. Appendix B: Flow Structure Differentiation Algorithm (MATLAB)	76

III. Index of Tables and Figures

i. Figures

Figure 1.1 - Schematic of PEM fuel cell components and operation. Not to scale	2
Figure 3.1 - Transparent fuel cell test system.....	17
Figure 3.2 - Anode and cathode channel geometry and dimensions (not to scale)	18
Figure 3.3 - Wavy channels on anode flow field/current collector.....	19
Figure 3.4 - Exploded view of test section assembly: (1) Lexan support piece, (2) rubber o-ring gasket, (3) current collector/flow fields, (4) PTFE gasket, (5) GDL (6) CCM.....	19
Figure 3.5 - Assembled transparent fuel cell	20
Figure 3.6 - Experimental setup: (a) transparent fuel cell, (b) Photron Ultima APX camera (anode), (c) Photron Fastcam 1024 camera (cathode), (d) motorized stage, (e) fuel cell test station, (f) temperature controllers.....	22
Figure 3.7 - Confocal laser scanning microscope images of (a) Freudenberg H2315 GDL and (b) Toray TGP-H-060 GDL	23
Figure 3.8 - Photron Fastcam Software used for simultaneous visualization of anode (left) and cathode (right) flow channels.....	26
Figure 4.1 - Representation of (a) digital image, and (b) digital video. The dotted squares represent the picture elements (pixels) of the image	28
Figure 4.2 - Common structuring elements (SEs) used in morphological processing: (a) cross, (b) square, and (c) disk. The black dots represent the origin of the SEs	29
Figure 4.3 - Erosion operation: (a) set A, (b), structuring element B, (c) erosion of A by B, with dotted line representing original set A	30
Figure 4.4 - Dilation operation: (a) set A, (b) structuring element B, (c) dilation of A by B with dotted line representing original set A	31

Figure 4.5 - Comparison of opening and closing operations: (a) set A, (b), structuring element B, (c) opening of A by B with dotted line representing original set A (d) closing of A by B with dotted line representing original set A32

Figure 4.6 - Pixel neighborhoods: (a) pixel p and its 4-neighbors, n, (b) pixel p and its 8-neighbors, n.....33

Figure 4.7 - Masking operation: (a) original image containing region of interest, (b) image mask, (c) array product of (a) and (b)34

Figure 4.8 - (a) Dry video frame, cathode window #1, (b) corresponding mask image, with white pixels representing channel area34

Figure 4.9 - Sample images from cathode window #1: (a) dry video frame, (b) test video frame, (c) resulting absolute difference image of (a) and (b)36

Figure 4.10 - Difference image from Figure 4.9(c) with different intensity regions highlighted. Dashed yellow outline indicates unchanged GDL, solid yellow outline indicates liquid water, and remaining non-zero intensity values represent condensation on channel surface37

Figure 4.11 - Thresholded difference image. The locations with liquid water possess denser pixel regions.....39

Figure 4.12 - Thresholded image after filling in holes40

Figure 4.13 - Area opening of thresholded image. Remaining connected components represent liquid water in the channels.....40

Figure 4.14 - Area opening image after hole filling and bridging operations41

Figure 4.15 - Closing of Figure 4.14 using disk structuring element41

Figure 4.16 - Final processed frame with faint reference frame added. Locations of liquid water in channels are represented by white pixels.....42

Figure 4.17 - Flow chart of video processing algorithm.....43

Figure 4.18 - Labeling of connected components in a binary image: (a) binary image, (b) corresponding pixel values of binary image, with 4-connected components highlighted, (c) resulting label matrix using 4-connectivity.....	45
Figure 4.19 - Flow chart of slug/film detection algorithm, with the first frame of a processed test video as the starting input.....	47
Figure 5.1 - Polarization curve and HFR for Freudenberg and Toray GDL samples. Stoich (an/ca) 1.5/2.5, 100% RH inlet gases.....	48
Figure 5.2 - Polarization curve and HFR for Freudenberg and Toray GDL samples. Stoich (an/ca) 1.5/5, 100% RH inlet gases.....	49
Figure 5.3 - Polarization curve and HFR for Freudenberg and Toray GDL samples. Stoich (an/ca) 3/8, 100% RH inlet gases.....	49
Figure 5.4 - Comparison of cathode window #2 for (a) Freudenberg and (b) Toray at stoichiometric ratio (an/ca) 1.5/2.5 and current density 100 mA/cm ²	51
Figure 5.5 - Comparison of cathode window #1 for (a) Freudenberg and (b) Toray at stoichiometric ratio (an/ca) 1.5/2.5 and current density 300 mA/cm ²	51
Figure 5.6 - Comparison of cathode window #1 for (a) Freudenberg and (b) Toray at stoichiometric ratio (an/ca) 1.5/2.5 and current density 500 mA/cm ²	52
Figure 5.7 - Comparison of anode window #2 for (a) Freudenberg and (b) Toray at stoichiometric ratio (an/ca) 1.5/2.5 and current density 200 mA/cm ²	52
Figure 5.8 - Comparison of cathode window #1 for (a) Freudenberg and (b) Toray at stoichiometric ratio (an/ca) 1.5/5 and current density 150 mA/cm ²	53
Figure 5.9 - Comparison of anode window #2 for (a) Freudenberg and (b) Toray at stoichiometric ratio (an/ca) 1.5/5 and current density 100 mA/cm ²	54
Figure 5.10 - Comparison of cathode window #1 for (a) Freudenberg and (b) Toray at stoichiometric ratio (an/ca) 3/8 and current density 100 mA/cm ²	55

Figure 5.11 - Comparison of cathode window #2 for (a) Freudenberg and (b) Toray at stoichiometric ratio (an/ca) 3/8 and current density 100 mA/cm ²	55
Figure 5.12 - Liquid water detection for cathode window #1 with Freudenberg GDL at stoichiometric ratio (an/ca) 1.5/5 and current density 50 mA/cm ² : (a) pre-processed image, (b) processed image.	56
Figure 5.13 - Liquid water detection for cathode window #2 with Freudenberg GDL at stoichiometric ratio (an/ca) 1.5/2.5 and current density 100 mA/cm ² : (a) pre-processed image, (b) processed image.....	56
Figure 5.14 - Liquid water detection for anode window #2 with Freudenberg GDL at stoichiometric ratio (an/ca) 1.5/2.5 and current density 100 mA/cm ² : (a) pre-processed image, (b) processed image.....	57
Figure 5.15 - Sequence showing capture and detection of dynamic slug movement in cathode channel #7 of window #1 with Freudenberg GDL at stoichiometric ratio (an/ca) 1.5/2.5 and current density 150 mA/cm ² . The dotted yellow line placed at the bottom of the slug highlights its travel.....	58
Figure 5.16 - Comparison of anode and cathode water coverage ratio for Freudenberg (left) and Toray (right) GDL samples, at stoichiometric ratio (an/ca) 1.5/2.5.....	59
Figure 5.17 - Comparison of anode and cathode water coverage ratio for Freudenberg (left) and Toray (right) GDL samples, at stoichiometric ratio (an/ca) 1.5/5.....	60
Figure 5.18 - Comparison of anode and cathode water coverage ratio for Freudenberg (left) and Toray (right) GDL samples, at stoichiometric ratio (an/ca) 3/8.....	61
Figure 5.19 – Distribution of liquid water among flow structures at stoichiometric ratio 1.5/2.5 for (a) Freudenberg anode flow field and (b) Freudenberg cathode flow field.	64
Figure 5.20 – Distribution of liquid water among flow structures at stoichiometric ratio 1.5/2.5 for (a) Toray anode flow field and (b) Toray cathode flow field. Note different scaling for water coverage ratio compared to Freudenberg GDL plots	65

ii. Tables

Table 3.1 - Lens properties for dual-visualization setup.....21

Table 3.2 - GDL material properties.....23

Table 3.3 - Fuel cell parameters for optical visualization experiments24

Table 4.1 - Summary of data classes28

Table 4.2 - Metrics calculated by video processing algorithm44

Table 5.1 - Freudenberg GDL water coverage ratio results.....62

Table 5.2 - Toray GDL water coverage ratio results62

Table 5.3 - Freudenberg GDL water distribution results66

Table 5.4 - Toray GDL water distribution results.....66

IV. Nomenclature

Abbreviations

PEM	Proton exchange membrane
GDL	Gas diffusion layer
CL	Catalyst layer
HFR	High frequency resistance
MEA	Membrane electrode assembly
PTFE	Polytetrafluoroethylene
RH	Relative humidity
MPL	Microporous Layer
NIST	National Institute of Standards and Technology
CCM	Catalyst coated membrane
PFSA	Perfluorosulfonic acid
OCV	Open circuit voltage
SE	Structuring element
GIMP	GNU Image Manipulation Program

Symbols

\dot{m}_{gen}	Rate of water production
i	Current density
A_{active}	Active area

F	Faraday's Constant
MW_{H_2O}	Molecular weight of water (18 g/mol)
\mathbb{Z}^2	2-D integer space
z	Set of all points in \mathbb{Z}^2
$A \ominus B$	Erosion of A by B (where A and B denote sets in \mathbb{Z}^2)
$A \oplus B$	Dilation of A by B
$A \circ B$	Opening of A by B
$A \bullet B$	Closing of A by B
α	Area (defined by number of pixels)
E	Connectivity of α
C_i	Connected components
N	Number of video frames
D	Dry video
P	Processed video
W	Test video
T	Threshold value

1. Introduction

Fuel cells continue to gain attention from automotive manufacturers as a potential alternative to internal combustion engines. Proton exchange membrane (PEM) fuel cells are the most favorable fuel cell technology for transportation applications due to their high power density, rapid start-up capability, and clean operation. Water management has been identified as one of the critical issues in the advancement of PEM fuel cells. Water is produced in PEM fuel cells as a byproduct of the electrochemical reaction, and can also be present due to the condensation from the humidified inlet gases. Although the presence of water is necessary in a PEM fuel cell to maintain sufficient membrane hydration, excess accumulation of liquid water within the cell, often referred to as flooding, can lead to mass transport losses and significant reduction in cell performance and durability [1].

A schematic of PEM fuel cell operation is shown in Figure 1.1. The source of water and associated two-phase flow in PEM fuel cells are the result of the following processes: first, hydrogen and oxygen (air) are introduced to the cell through the flow field channels on the anode and cathode sides, respectively. The gases then diffuse from the channels through the porous gas diffusion layer (GDL) to reaction sites at the catalyst layer (CL). On the anode side, hydrogen is oxidized to produce H^+ ions which are then transported through the membrane. Only protons can pass through the membrane, and the electrons are forced to flow around the fuel cell through an external circuit thus creating the usable electricity. After passing through the external circuit, the electrons recombine with the H^+ ions and oxygen at the cathode CL producing water. The product water is then transported back through the GDL and into the flow field channels in liquid and/or vapor form (depending on fuel cell operating conditions), where it is then removed from the channels via gas flow.

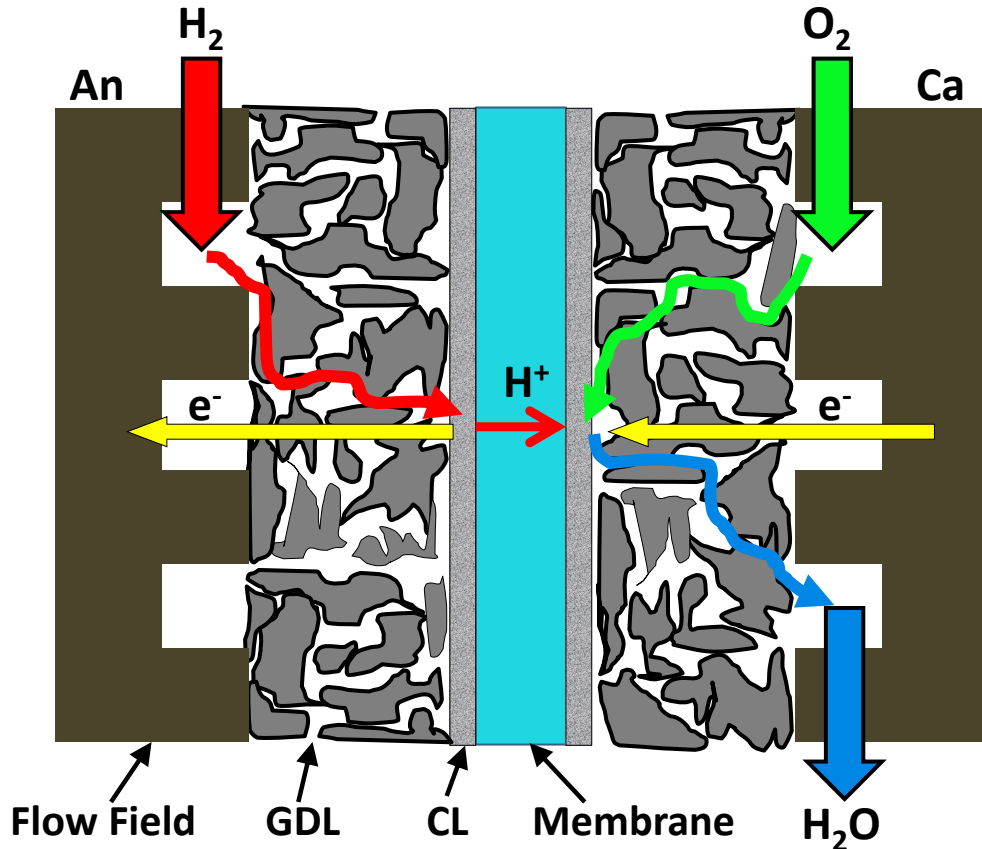
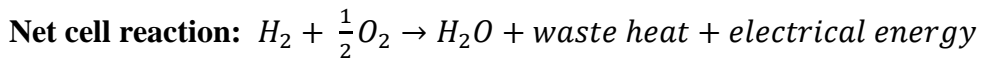
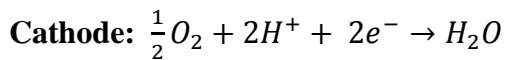
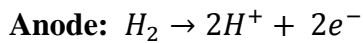


Figure 1.1 - Schematic of PEM fuel cell components and operation. Not to scale.

The reactions that take place in the cell are as follows:



The rate of water generation in the cell, from Faraday's Law, is expressed in Equation (1.1) as

$$\dot{m}_{gen} = \frac{iA_{active}}{2F} MW_{H_2O} \quad (1.1)$$

where \dot{m}_{gen} is the rate of water production, i is the current density, A_{active} is the active area, F is Faraday's Constant and MW_{H_2O} is the molecular weight of water.

In the case of channel/flow field flooding, excess liquid water accumulates within the flow field channels to form water films which partially block channels, or columns of water which span the entire channel width called slugs, which can block or hinder the flow of reactants and their diffusion through the GDL to the catalyst layer. This can lead to a reduction in the electrochemically active surface area, which limits the reactions that can take place and decreases cell performance. The presence of slug flow in the gas channels is therefore undesired. In addition, blocked or partially blocked gas channels can lead to flow maldistribution among parallel flow field channels, and increased channel pressure drop. Flooding can be especially prevalent at lower temperatures and lower reactant flow rates (lower power operation), when the gases may not be able to remove the liquid water from the channels. An accurate assessment of the total amount of liquid water present in the anode and cathode gas channels and its flow structure is therefore crucial in assessing performance losses induced by water accumulation in the flow field, and to the development of water management and purge strategies.

Optical visualization using a fuel cell with transparent components is a popular technique used to observe PEM fuel cell flow channels during operation. There are, however, limited optical visualization studies that are able to obtain quantitative data pertaining to the amount of liquid water accumulation in the flow field channels, or the two-phase flow structure. Of these studies there are no automated techniques for water quantification, and the results must be obtained through manual observation and selection, which can be tedious, time-consuming, and is subject to inherent human errors. Manual selection may also fail to capture the presence of dynamic liquid water in the channels. In addition, many studies use rather arbitrary channel dimensions, which may not be representative of actual full scale fuel cell geometry. The majority of work also tends to focus on cathode channel observation, although flooding can be just as prevalent on the anode side.

The objective of this study was to develop a technique to automatically detect and characterize the two-phase flow present in a transparent fuel cell during operation using direct optical visualization and image processing. The small scale transparent cell design used in this work emulates geometry seen in full scale PEM fuel cells. A dual-visualization setup was designed to allow for simultaneous observation of the anode and cathode flow

channels, and high-speed cameras were used to record the two-phase flow in the gas channels. A video processing algorithm was developed in order to automatically detect static and dynamic liquid water in the fuel cell channels and yield information pertaining to its quantity and flow structure. This technique can be used to obtain data for model validation purposes, and can also be used towards the optimization of cell operational parameters and material sets for water management. The simultaneous anode and cathode visualization technique can be used to further the understanding of water transport across the membrane.

2. Literature Review

Water management has recently emerged in the literature as a key research area in the development of proton exchange membrane fuel cells for automotive applications. Liquid water comes from two processes in a proton exchange membrane fuel cell – the oxygen reduction reaction that takes place on the cathode electrode, and condensation of water from the humidified fuel streams. The presence of water in a PEM fuel cell is necessary to sustain membrane hydration and ionic conductivity, but excess water accumulation can lead to flooding of the cell and a reduction in performance and durability [1-8]. Flooding can severely hinder the flow of reactants and block reactant sites thus limiting cell performance, and it can also cause an uneven distribution of reactants and thus non-uniformity in current and temperature distributions within the cell and promote material degradation. In addition, excess water accumulation prior to cell shut-down can require extended purge sequences [5]. The major types of PEM fuel cell flooding that have been identified are catalyst layer/gas diffusion flooding, and flow field/channel flooding. In catalyst layer/GDL flooding an accumulation of liquid water within these layers blocks pores and reduces the number of active reaction sites. In flow field/channel flooding, two-phase flow within the channels can hinder the flow of reactants and their diffusion through the GDL, limiting cell performance due to mass transport losses and a reduction of the electrochemically active surface area. Typically the cathode side of the cell is studied for water management because of its role in water production, but the anode side can also be prone to flooding [5, 6, 9-12].

Although water production does not take place on the anode side by the same means as it does on the cathode side, it has been shown that liquid water is present on the anode side as a result of two processes – transport from the cathode side of the cell, and humidification of the hydrogen gas stream [9, 11]. Water transports from the cathode side to the anode side as a result of back diffusion, which is a concentration gradient driven flux through the membrane. Anode flooding can be detrimental to the operation of PEM fuel cells because once water accumulates on the anode side it is not as easily removed due to the lower hydrogen flow rates, and it can also lead to carbon corrosion in the cathode catalyst layer due to localized fuel starvation [9].

Two-phase flow in the gas channels is a critical aspect of fuel cell water management [1, 3, 4]. The presence of excess liquid water in the channels can have detrimental effects such as: restricted access to reaction sites caused by a liquid film on the GDL surface, starvation of reaction sites due to partial or complete blockage of the gas channel, maldistribution of reactant flow and subsequent non-uniform current distribution, and an increase in channel pressure drop as a result of liquid water blockage [1].

In order to better understand flooding in the channels and its effect on fuel cell performance, a variety of diagnostic tools have been employed to detect as well as characterize the liquid water within a fuel cell including: cell voltage and high frequency resistance (HFR) measurements [10, 13], pressure drop measurements [8, 13-16], and visualization [5-26]. Of these techniques, visualization has the advantage of obtaining information regarding the location and spatial distribution of liquid water in the anode and cathode flow fields, GDL, and membrane electrode assembly (MEA), as well as water transport dynamics and two-phase flow structure. Two of the most prominent methods of visualization are neutron radiography and direct optical visualization in the visible range. Neutron radiography is a non-invasive technique used to visualize and quantify the presence of liquid water in flow field channels, within the gas diffusion layer and MEA, and under the land area [5, 6, 19, 20, 22]. In the neutron radiography technique, a beam passes from a neutron source through an operating fuel cell, and the attenuation of the beam reveals the two-dimensional measurement of water thickness. The 2-D nature of neutron radiography makes distinguishing cathode water from anode water rather ambiguous, as it is difficult to determine which layer of the cell the water is residing in (anode flow fields, MEA, cathode flow fields, etc.) It is also limited by its current spatial and temporal resolutions (approximately 25 μm and 5.4 s, respectively [27]) which makes it unable to resolve water transport dynamics, although efforts are underway to improve resolution. Neutron radiography has severe limitations in visualizing small, fast-moving water quantities; in addition, calibration errors can lead to less accurate water measurements in operating cells [6]. The technique is further limited by its high cost and limited facilities [28]. Optical visualization, which requires the development of transparent fuel cell components to view the internal channels, is a lower cost alternative that offers the advantage of high spatial and temporal resolutions which enables the capture of highly localized two-phase flow dynamics present in the cell channels. This knowledge can

be used to enhance cell design and material selection, as well as give insight to optimal conditions for purge and operation, and therefore makes optical visualization an ideal candidate to study two-phase flow within the gas channels and at the GDL surface [6-9, 11, 13-18, 21, 23-26].

Tuber et al. [23] was the first group to utilize direct optical visualization to study the accumulation of liquid water in cathode channels at low temperatures. They developed a transparent fuel cell consisting of two air channels separated by a stainless steel rib. The channel dimensions were 1.5 mm width, 1.0 mm depth, and 50 mm length. They performed constant voltage tests at low temperature (30 °C) and ambient pressures and observed the liquid water in the cathode channels. Observations were recorded using a digital camera. The effect of the liquid water on cell performance was investigated by monitoring the drop in current density due to the accumulation of liquid water in the air channels. In addition, the effect of GDL hydrophobicity was studied. It was determined that a change in the surface properties of the GDL in either direction (more hydrophilic or more hydrophobic) resulted in a substantial change in water accumulation tendencies in the channels. They concluded that in the case of low temperature and cold-start conditions, hydrophilic GDLs are more beneficial for fuel cell performance due to more uniform distribution of water content in the MEA.

In 2004, Hakenjos et al. [17] developed a cell to simultaneously measure current and temperature distributions while observing flow field flooding. The anode flow field was segmented to measure the cell current distribution, and an infrared (and optical) transparent window was used on the cathode side. A CCD camera was used to record observations of liquid water on the cathode. The cathode flow field had channels of 1 mm wide by 2 mm deep with 1 mm spacing in between. Toray GDL with a thickness of 360 μm was used in their tests and a constant voltage of 200 mV was sustained for 1 hour prior to measurements. Dry hydrogen was supplied to the cell at 100 sccm, and humidified air was supplied to the cathode ranging from 250 to 750 sccm. In general, the cell current rose with increasing air flow rate, and temperature increased as well due to the higher reaction enthalpy. The authors found that condensed water lead to lower current density due to blockage of gas flow and reaction sites, but contrary to their expectations the temperatures were found to be higher at

flooded sections compared to non-flooded regions. This was attributed to the enthalpy of water condensing causing an increase in the temperature.

Also in 2004, a transparent fuel cell was developed by Yang et al. [26] that was suitable for testing under higher temperatures (70 °C), higher current densities, and fully humidified inlet gas streams. The test section comprised of two clear polycarbonate plates sandwiching gold plated stainless steel current collectors/flow fields and the MEA. The anode and cathode flow fields were identical and consisted of seven straight parallel channels with geometry of 1 mm x 1 mm by 100 mm. The active area for the cell was 14 cm². The visualization studies were conducted on the cathode side of the cell and a Sony digital camcorder and 24x microscopy lens were used for recording observations. The emergence of water droplets from preferential pores on the GDL surface was observed during their testing. Other observations included water film on the channel walls, and a water bridge across the width of the channel that blocked gas flow. This caused a notable decline in the average current density, indicating the negative effect the blockage of gas flow channels can have on cell performance. They concluded that under practical stoichiometric ratios, the two-phase flow in the cathode channels of their cell was in the form of annular film flow.

Zhang et al. [7] used a transparent fuel cell to characterize liquid water removal in a PEM fuel cell from both the GDL surface and the gas flow channels. The cell was 14 cm² with 100 mm long x 1 mm wide x 0.5 mm deep flow channels. A polycarbonate window was used to have visual access into the cell and images were recorded using a 3-CCD camera. Toray 090 GDL was used with 20% wet-proofing and the cell was operated at 80 °C with fully humidified gas streams. The main modes of water removal were determined by this group to be: mist flow (tiny water droplets suspended in the gas stream) at high air flow velocities, corner flow (along interior channel corners due to capillary wetting), annular film flow (water film along channel sidewall), and slug flow (water band clogging the gas channel) at low velocities. Corner flow was found to be the primary liquid water removal mechanism and it was concluded that steady corner flow is an efficient way to remove water from the channel. This group also studied droplet formation and on the GDL and used image processing tools to determine the fractional coverage of liquid droplets on the GDL surface. Water removal from the GDL was determined to be due to either drag force from the gas

flow (high velocity) or capillary interactions with the channel walls. The forces acting on a water droplet on the GDL surface were modeled, and they determined the droplet detachment diameter to be an important design parameter. A channel size smaller than the droplet detachment diameter resulted in the water contacting the channel walls before it detaches from the GDL surface, which could promote liquid water buildup in the channels.

In 2007 Ge and Wang [9] were the first to use a transparent fuel cell to investigate liquid water formation and transport on the anode side of a PEM fuel cell. The cell design was the same used in previous experiments by Yang et al. [26]. The GDL used on the anode side was Toray 060 with microporous layer (MPL), and treated (polytetrafluoroethylene - PTFE) and untreated samples were used. Both a straight channel flow field (14 cm^2) and four-pass serpentine flow field were used (5 cm^2). An Olympus DP 70 digital camera with a Navitar zoom lens was used. Experiments were performed in a parallel channel flow field at three different current densities – 0.2, 0.5, and 0.8 A/cm^2 – and inlet gas relative humidity (RH) of 66%. At the lowest current density, condensation and film were present in the anode channel but significant flooding was not observed. At the higher current densities, no film or condensation was observed in the channel and the authors concluded that anode flooding was strongly dependent on current density. At 0.2 A/cm^2 , hydrogen stoich ratios of 1.5, 2.0, and 3.0 were tested and it was determined that hydrogen flow rates do not have a significant effect on the formation and transport of water in the anode. Ge and Wang further measured the anode pressure gradient and saw that a sharp increase in pressure gradient correlated to liquid water blocking several of the channels. Using the anode pressure gradient they were able to confirm that channel clogging can be mitigated by using a hydrophilic GDL on the anode side. Additional tests with a four-pass serpentine cell verified that anode side flooding can be diagnosed using the anode pressure gradient. Since no water droplets were found on the anode GDL in any of the tests it was determined that, in contrast to the cathode water production mechanism, water vapor condensation is the source for liquid water formation on the anode – either from the cathode side via membrane transport or from the hydrogen gas stream as consumption of hydrogen leads to supersaturation in the anode gas.

Optical visualization experiments were conducted by Spornjak et al. [11] to investigate two-phase flow dynamics in conjunction with the effectiveness of water transport for different

GDLs. A transparent single channel (1 mm) serpentine cell was tested at high temperature and high water production rates with different commercially available GDLs – Toray 060 carbon paper, Sigracet wet-proofed SGL31BA (without MPL), SGL31BC and SGL35BC (with MPL), and a Ballard woven cloth GDL (AvCarb™ 1071HCB). Liquid water was found to originate in the cathode either by being wicked away through GDL pores into the channel, from condensation on the channel walls, or from bursts of liquid water from the fuel cell test stand. They also observed mechanisms of water transport within the flow field and found that droplets were either removed from the GDL surface via the gas stream, consumed by other moving droplets, film, or slugs from upstream, or contacted the channel walls and moved through the channel as film or slug flow. At the U-turns and corners of the serpentine channel water accumulation was more prevalent and resided for longer periods of time. In addition, because of the dynamic nature of water coverage and removal along the channels, they found that the active area of the cell will change as reactant sites are blocked by flooding. The effect of GDL materials and their water management properties revealed that with the wet-proofed SGL GDLs, discrete droplets emerged over the entire visible surface area. This was in contrast to the untreated GDLs where the water typically moved along the sidewall in the form of film or slugs. Toray GDL had lower performance and hardly any visible water at the same water production rates, and the authors concluded that the untreated GDL cannot efficiently push the water to the membrane through the catalyst layer or eject water into the gas channels. This resulted in low membrane hydration, blockage of pores and hindrance of gas flow. The anode side of the cell was visualized to study effect of the microporous layer. Results revealed that the MPL had an effect on water dynamics and lead to an increase of water content present on the anode side. This was attributed to the MPL creating a pressure barrier at the cathode catalyst layer which causes the water to be pushed to the anode side. The anode water was determined to be caused by water transport from the cathode to anode across the membrane and by the humidified gas stream.

Liu et al. [8, 15, 18] performed several studies to characterize flooding and pressure drop in the cathode channels of a PEM fuel cell. In 2007 this group investigated the relationship between water flooding and pressure drop in a PEM fuel cell by studying the effect of cell temperature, current density, and operating time on the total pressure drop for the anode and cathode sides [15]. A 5 cm² transparent PEM fuel cell was used with channel dimensions of

0.8 mm wide by 24 mm long by 1 mm deep. The cell was tested at 35 °C and 70 °C and the two-phase flow in the anode and cathode flow fields was also observed. Their results showed that the cell performance was reduced due to the presence of liquid water in the channels because of mass transport limitations. The total pressure drop of the cell was found to primarily depend on the amount of resistance to gas flow caused by water in the channels. The total pressure drop was found to increase with increasing current density, but decrease with an increasing cell temperature. Overall, cathode flow field pressure drop was higher than anode flow field pressure drop. A ‘rate of flooding’ parameter (R_f , %) was introduced in an effort to quantify flooding as the ratio of the length of water columns in the channels to the length of the channels.

In 2008 the same group also studied the effect of cell temperature, cathode flow rate, and operating time on the two-phase flow patterns and liquid in the cell [8]. They observed that increasing the cell temperature caused a decrease in condensation, and an increase in electrochemical reaction kinetics, which led to better fuel cell performance. However, too much of a temperature increase can have an opposite effect by drying out the membrane and reducing performance. An increase in the flow rate on the cathode side corresponded to an increase in cell performance by aiding in the removal of liquid water from the flow field, but a threshold condition was reached at a stoich ratio of 42.9 when membrane dehydration caused a decrease in performance. They clearly observed slug flow at low gas flow rates and annular flow at higher flow rates, and a transition pattern between the two was also observed at intermediate air flow rate. Blockage of channels by liquid water columns lead to poor performance due to mass transfer losses.

Owejan et al. [5] highlighted the need for better understanding of two-phase transport under low temperature and low power conditions. U.S. Department of Energy performance targets were used in their design of a 50 cm² fuel cell for neutron radiography testing. The resulting 22 cathode channels were 0.7 mm wide by 0.4 mm deep channels and 0.5 mm lands, and the 11 anode channels were scaled to 1.5 mm lands and identical channel geometry. The channel length was 183 mm. The flow fields were designed to have a wavy pattern in order to mitigate compression misalignments. They performed a number of steady state tests at NIST to measure water distributions within the cell for a wide range of temperatures. The results

showed that lower operating temperatures contained higher amounts of liquid water, especially at lower current densities. This is important because as the authors point out, a fully dynamic automotive fuel cell mostly operates at 20% of its rated power, and many trips aren't long enough in duration to bring the fuel cell up to its designed operating temperature. They also identified areas that may present problems during start-up in freezing conditions, including the anode channels and the channel-to-header transitions at the exits. The transport processes that occur in the cell during a shut-down purge sequence were also investigated. Two main water removal regimes were identified when the cathode was purged with air: first the anode channel water was cleared rapidly due to a system pressure release, and then the water residing in the gas diffusion layers was evaporated slowly. These results showed that at low shut down temperatures, long cathode air purges may be necessary to ready the cell for start-up in freezing conditions.

In 2009 Spornjak et al. [6] introduced a novel visualization technique combining neutron radiography and direct optical visualization in order to quantify the water in a PEM fuel cell during operation. The goal of this study was to provide a technique that allows one to obtain and separate MEA and flow field water content. It also attempts to differentiate anode and cathode channel water transport. A 25 cm² fuel cell [11] was observed simultaneously by neutron radiography and optical visualization through the use of a silver-coated quartz mirror. Three alternate versions of the cell were tested – a non-transparent cell, a cathode transparent cell, and anode transparent cell. A Nafion membrane was tested in two cases – with Toray 060 GDL on both sides of the cell, and with SGL35BC and SGL31BA GDL on the cathode and anode respectively. For different test cases the neutron images were overlaid onto the optical image. Information relating the water in the channels to the neutron image was found by comparing the dry optical image and wet optical image to the overlay. When observing the cathode side, some areas of high neutron attenuation could not be correlated to visible water present in the cathode flow field. Using this comparison it was possible to deduce that the water remaining is located in the MEA and anode channels. The authors speculate that with further image processing and assumptions it may be possible to determine the upper and lower bounds for the water content in these regions. With no anode water present it was possible to distinguish and quantify the cathode water from the MEA water, however to date, it is still a challenge to discern water distributions between individual cell

components. This group's use of concurrent optical and neutron radiography images gave more complete information about cell water distribution, and helped to make improved correlations between cell performance and water dynamics.

In 2009 Hussaini and Wang [13] used the same transparent cell design outlined by Yang et al. [5] to perform in situ visualization of cathode flooding. The cell was operated with a Teledyne test station and an Olympus video microscope was used to record observations. A 200 μm thick Toray GDL was used for testing at a temperature of 80 $^{\circ}\text{C}$, relative humidities of 26%, 42%, and 66%, current densities of 0.2, 0.5, and 0.8 A/cm^2 , and flow stoichiometries of 2, 2.5, 3, 3.5 and 4. From their visualization they were able to observe cathode channel flooding to be concentrated towards the exit region. In addition, due to low gas flow rates, the level of flooding was higher at low current densities and stoichiometries. The main flow patterns they observed in the channels were single-phase, droplets, film, and mist flow. This information was used to construct a flow pattern map depicting the flow transition regions as a function of superficial air and liquid water velocity, which can be useful for both cell design and determining optimal operation conditions to minimize flooding. Two other parameters were introduced by this group to aid in the understanding of flooding in the channels – the two-phase pressure drop coefficient and wetted area ratio. The two-phase pressure drop coefficient was defined as the measured pressure drop during cell operation divided by the single phase pressure drop, and analyzing this parameter showed that flooding in the channels can cause as much as a four-fold increase in total pressure drop. In order to better quantify the amount of liquid water present in the channels, the wetted area ratio was developed. This is the ratio between the total area within the channels where two-phase flow is consistently present and the total area. This was done by manually selecting the area of the channels that was perceived to be occupied with two phase flow, a technique that lends itself to inherent uncertainty and error. The wetted area ratio was shown to be relatively constant for a given operating condition even though the distribution was varied. They noted that this parameter could be more refined by developing image processing techniques to more accurately assess the wetted channel area without bias caused by manual selection.

Yamauchi et al. [29] simultaneously observed the anode and cathode of a transparent cell (referred to as two-pole simultaneous measurement) in order to test different anode and

cathode flow orientations and their effect on water management. A 3-serpentine channel was used for the flow fields. A condensation rate parameter was used for quantifying the water in the flow fields, and was defined as the ratio of area in the channels where condensate forms to the total area. The authors observed anode flooding at low humidities due to water transport across the membrane. It was found that asymmetrical flow orientations (e.g. anode top/cathode bottom, anode bottom/cathode top) promoted water transport between the anode and the cathode.

In 2010, Spornjak et al. [30] expanded their simultaneous neutron and optical imaging work [6] and compared the water content and dynamics of three different flow field types: parallel, single-serpentine, and interdigitated. Anode channel flooding was observed in all tests, and water was removed from the anode at a much slower rate due to the lower flow rates. Anode flooding was contributed primarily to water transport across the membrane as a result of the microporous layer present on the cathode side. In addition, liquid water was observed in the anode channels sooner than the cathode channels. The parallel flow field was found to exhibit the worst performance, and possessed the highest water content. The main method for water removal in this type of flow field was determined to be short slugs being purged from the cell periodically as they interacted with other water droplets and the channel walls. Flooding was observed on both the anode and cathode at higher current densities. The single-serpentine flow field maintained the lowest water content during operation, and exhibited the highest pressure drop. The interdigitated contained much higher water content than the single-serpentine, but maintained comparable performance. The water removal mechanisms and distribution in this type of flow field were found to be similar to the parallel channel flow field.

2.1. Summary of Research Needs

It can be seen from the literature that direct optical visualization is a powerful tool that can enhance the fundamental understanding of two-phase flow in PEM fuel cell gas channels. One key area lacking in the literature is the ability to generate quantitative data pertaining to the liquid water observed in the fuel cell channels without relying on manual selection of wetted regions [13, 29], which inherently lends itself to error and bias and may not capture dynamic cell water. In addition, there is no technique that can automatically discern among

the flow structures of the liquid water in the channels. Currently in the literature there has been a minimal amount of visualization studies aimed at better understanding anode flooding dynamics [6, 9, 11], and studies performing optical visualization of both the anode and cathode simultaneously are extremely limited [29]. In addition, most studies (with the exception of [5]) use rather arbitrary channel and flow field geometry for small scale visualization testing, with little design influence from actual full scale fuel cell hardware. Relatively low temperature/power conditions, which are pertinent to realistic automotive fuel cell drive cycles [5], can be especially prone to flooding and further insight into liquid water accumulation under these conditions would be beneficial.

2.2. Scope of Work

The goal of this research is to develop a technique to characterize and quantify the two-phase flow in the gas channels of a PEM fuel cell using optical visualization. The following objectives are established in order to accomplish this goal and address the current research needs:

Objective 1 – Small Scale Transparent Fuel Cell with Realistic Geometry

Implement a small scale (50 cm²) transparent fuel cell that represents actual full scale automotive PEM fuel cell hardware for in situ optical visualization experiments.

Objective 2 – Simultaneous Anode and Cathode Flow Field Visualization

Develop a dual-visualization system that allows for concurrent viewing and recording of two-phase flow activity in the anode and cathode flow field channels using high-speed cameras.

Objective 3 – Automatic Detection and Quantification of Static and Dynamic Liquid Water in Fuel Cell Gas Channels

Develop a video processing algorithm in MATLAB® that can automatically detect liquid water in the flow field channels from recorded test videos and yield quantification information.

Objective 4 – Automatic Differentiation of Two-Phase Flow Structure

Develop a video processing algorithm in MATLAB that can automatically determine the flow structure (e.g. slug, film) of detected liquid water in the channels and yield information pertaining to the distribution of water among the different flow structures.

3. Experimental Methodology

3.1. Overview of Experimental Work

In this work, a transparent PEM fuel cell with visual access to both the anode and cathode sides was developed for use with optical visualization techniques. The geometry of the cell was designed to represent actual automotive fuel cell hardware. A high speed camera system was used to simultaneously observe the two-phase flow in the anode and cathode gas channels of the fuel cell during operation. This in situ experimentation allowed for information pertaining to liquid water quantification, distribution, transport dynamics, and two-phase flow structure to be extracted. Additional performance metrics such as polarization curve and HFR measurements were also recorded. This method was used to compare two GDL samples from a water management perspective. Tests were performed at 35°C for a range of current densities and stoichiometric ratios to elucidate two-phase flow dynamics at lower temperature/low power conditions, when excess liquid water in the cell can be especially prevalent.

3.2. Experimental Setup

3.2.1. System Overview

The fuel cell testing was performed using a Hydrogenics G40 fuel cell test station operated under constant current mode. The fuel cell was mounted in a vertical down position with co-flow orientation. Air and hydrogen were supplied to the cell through the test station from a Parker Balston Zero Air Generator and bottled hydrogen, respectively. The water for the gas humidification system was supplied from a Siemens water de-ionization system. The inlet gas temperatures, humidities, and flow rates were regulated by the Hydrogenics test station, which also monitors cell voltage and membrane hydration (HFR). The temperature of the fuel cell was controlled using Watlow flexible silicone heaters attached to the cell endplates. The inlet gas tubes were heated with OMEGALUX® rope heaters to prevent condensation and maintain a constant gas temperature from the test station to the cell inlets. Both the cell heaters and rope heaters were controlled using Omega CN1504-TC temperature controllers. The internal cell temperature was monitored using four 0.05 mm thick Omega 88309K thin leaf-type thermocouples embedded within the cell. The internal cell temperature measurements were recorded using a National Instruments data acquisition system (NI

cDAQ-9172) and a LabVIEW VI. A Velmex 3-axis motorized stage mounts two Photron high-speed cameras, each facing one side of the transparent fuel cell. The fuel cell assembly and visualization equipment were mounted to a Newport ST-UT2 vibration isolation table. A schematic of the experimental setup is shown in Figure 3.1.

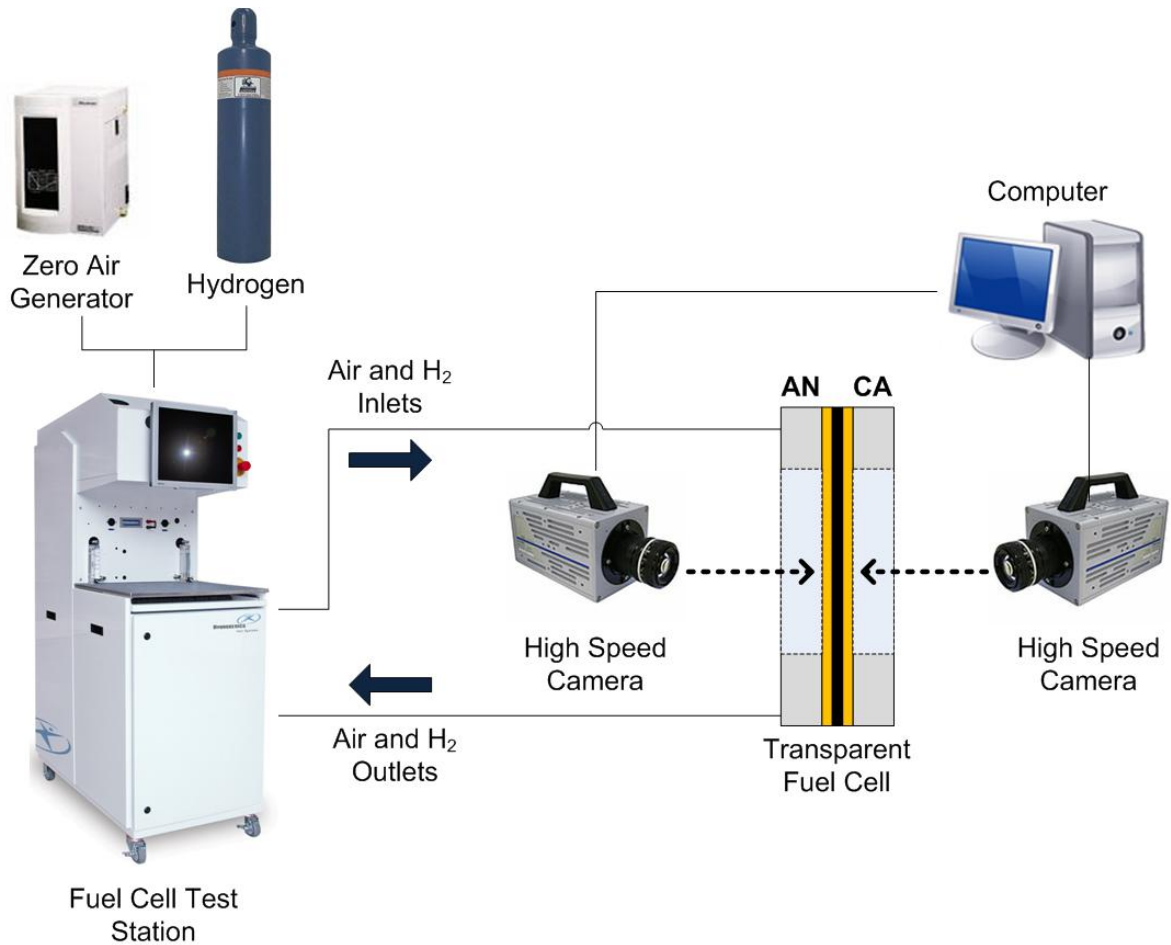


Figure 3.1 - Transparent fuel cell test system.

3.2.2. Transparent PEM Fuel Cell Design

The design of this 50 cm² transparent fuel cell used in this work has previously been described in literature [5, 31] and the details are summarized in this section. The test section is comprised of anode and cathode flow fields sandwiching the gas diffusion layers (GDLs) and catalyst coated membrane (CCM). The flow fields of this cell also function as the current collectors and are formed by 0.4 mm thick gold plated copper plates. Copper was chosen because of its high electrical conductivity and receptiveness to gold plating, which has been applied in order to minimize corrosion. The anode and cathode flow field channels were

machined through the copper plates resulting in a channel depth of 0.4 mm. Lexan® (polycarbonate) support pieces provide optical access to the flow field channels and form the channel bottoms (surface opposite of the GDL) when the test section is assembled. The channel geometries and dimensions were designed by Owejan et al. [5] in order to meet Department of Energy targets for volumetric power density. The rectangular cathode channels are 183 mm long and 0.7 mm wide with 0.5 mm wide lands between adjacent channels. The channel and land width dimensions were based on values from the literature that were found to be optimal for cell performance. The anode channel geometry is identical to the cathode except that the land width is scaled three times larger in order to account for the higher binary diffusion coefficient of hydrogen, resulting in 1.5 mm lands. The anode and cathode channel geometries are shown in Figure 3.2.

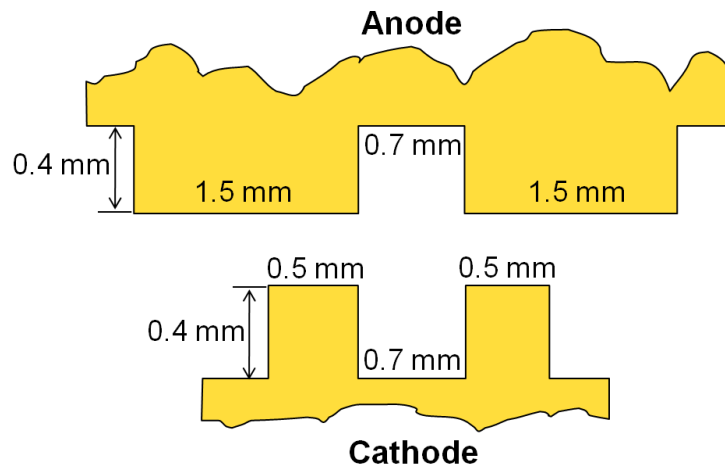


Figure 3.2 – Anode and cathode channel geometry and dimensions (not to scale).

An active area of 50 cm² results in flow fields comprised of 22 cathode channels and 11 anode channels. The channel depth was minimized to preserve volumetric power density target constraints while avoiding the negative effects of GDL intrusion/inflection into the channel under compression, which are exacerbated as the channel depth decreases. The channel length of 183 mm was extracted from active area calculations to meet fuel cell power targets. In order to avoid misalignment effects and mechanical shearing of the GDL associated with straight channels, a wavy channel pattern was implemented, as shown in Figure 3.3.

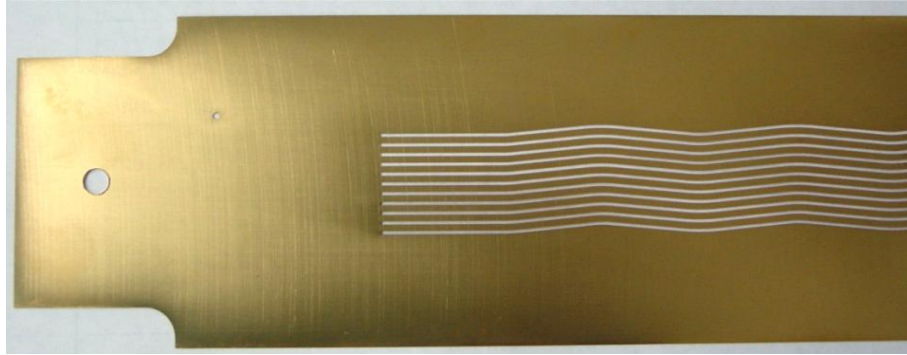


Figure 3.3 – Wavy channels on anode flow field/current collector.

The assembled test section contains a CCM that is sandwiched by gas diffusion layers, anode and cathode flow fields, and the Lexan support pieces. The MEA consists of the anode and cathode GDLs and the CCM. PTFE and rubber o-ring gaskets are placed appropriately between components. An exploded view of the test section is shown in Figure 3.4.

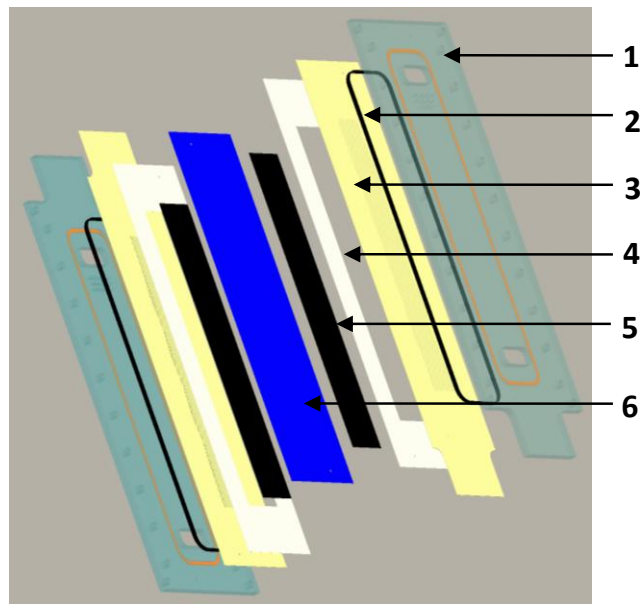


Figure 3.4 - Exploded view of test section assembly: (1) Lexan support piece, (2) rubber o-ring gasket, (3) current collector/flow fields, (4) PTFE gasket, (5) GDL (6) CCM.

The flow fields are carefully assembled to ensure channel width and uniformity, and dowel pins are used to ensure the proper alignment of each cell component during assembly. The test section is housed on both sides by machined 6061 aluminum blocks which are used to compress the cell and also contain the inlet and outlet manifolds for the fuel streams. The aluminum end pieces contain a series of windows (machined-through cavities) for viewing

access through the transparent Lexan pieces. Rubber o-ring gaskets are used to seal the area between the test section and aluminum blocks. The entire cell assembly is compressed to 200 psi. Even compression distribution within the cell was verified prior to testing by replacing the soft goods with a pressure sensitive film. The fully assembled cell is shown in Figure 3.5.

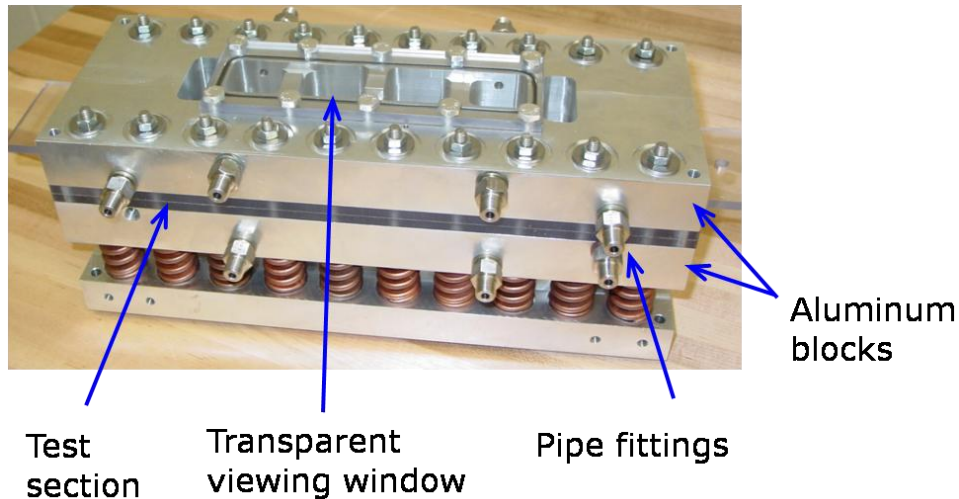


Figure 3.5 – Assembled transparent fuel cell.

3.2.3. Dual-Visualization Setup

A dual-visualization setup was developed in order to perform simultaneous optical visualization of the anode and cathode sides of the fuel cell during operation. The setup consists of two high speed video cameras – a Photron Ultima APX (anode side) and Photron Fastcam 1024 PCI (cathode side). The Ultima APX has a full 1024x1024 megapixel resolution for a frame rate range of 60-2,000 fps, and the Fastcam 1024 PCI has full 1024x1024 for 60-1,000 fps. A Sigma Macro 105mm F2.8 EX DG lens is attached to the Ultima APX and used for viewing the anode side of the cell, and a Nikon 105 mm AF Micro Nikkor lens is used on the Fastcam 1024 to visualize the cathode. The lenses share nearly identical specifications, as shown in Table 3.1, which allows for spatially comparable images of both sides during visualization.

Table 3.1 - Lens properties for dual-visualization setup.

Lens Property	Sigma Macro 105 mm F2.8 EX DG (Anode)	Nikon 105 mm AF Micro Nikkor (Cathode)
Focal Length	105 mm	105 mm
f/Stop Range	2.8 - 32	2.8 - 32
Minimum Focus Distance	0.310 m	0.314 m
Magnification	1:1	1:1
Angle of View	23° 18'	23° 20'

Edmund MI-150 fiber optic illuminators provide lighting to the cell viewing windows. A single aluminum bracket mounts both cameras to a Velmex motorized 3-axis stage which has a positional repeatability of 5 microns. The design of the mounting bracket allows the cameras to vertically traverse the length of the flow field channels while maintaining simultaneous view of the same window on respective sides of the cell. The cathode side camera is connected to the mounting bracket with a manually controlled Velmex linear slide in order to enable additional flexibility with focusing the cameras or for use with alternate lenses with different focal ranges. The dual-visualization setup is shown in Figure 3.6.

The motorized stage is moved by stepper motors which are controlled through MATLAB. A MATLAB code was developed to store the vertical position of each window (1-4) from a zero reference point (absolute bottom of the vertical stage) and mathematically relate this position to each of the other windows. This ensures that the cameras will automatically return to the same position for each specified window regardless of their previous location. When the code is run, the cameras automatically move to the zero reference point, and the user is prompted to enter a window number. After a window number is entered the cameras move to that position and the user is again prompted to enter a window number, and the sequence repeats until the code is terminated by the user.

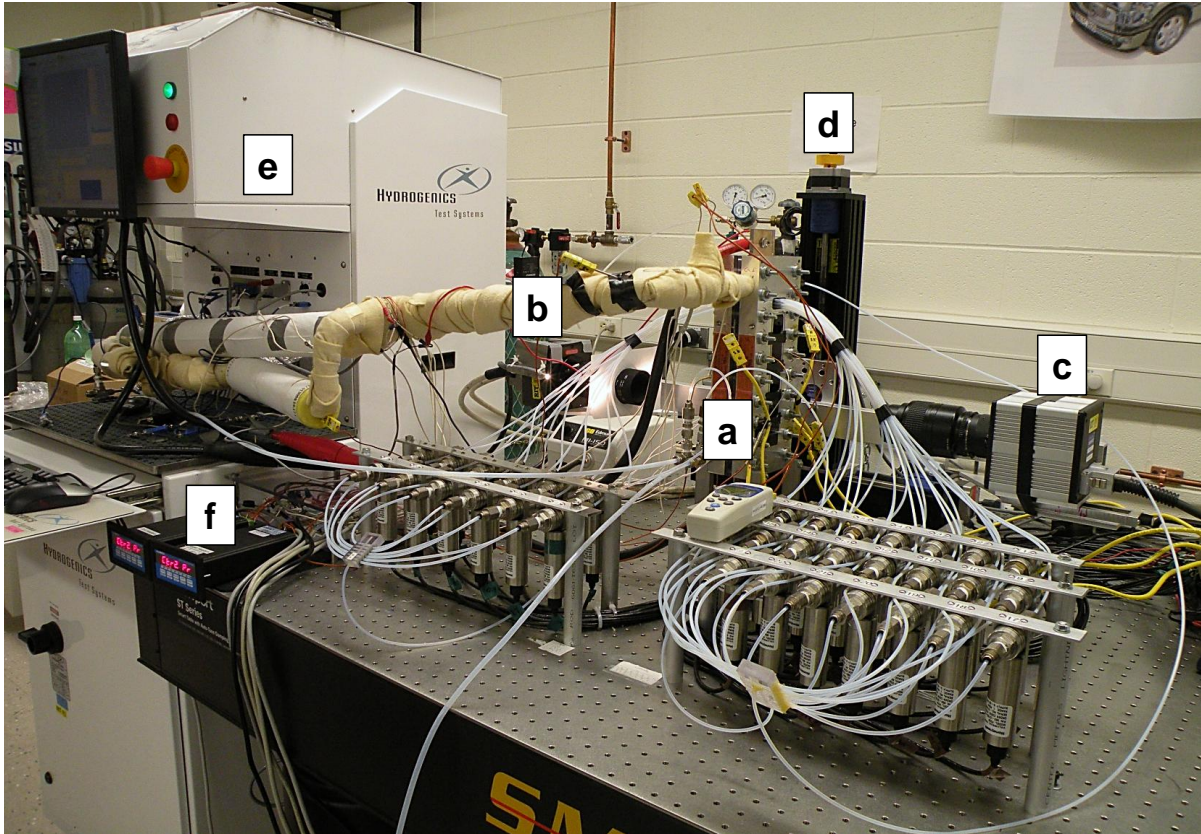


Figure 3.6 - Experimental setup: (a) transparent fuel cell, (b) Photron Ultima APX camera (anode), (c) Photron Fastcam 1024 camera (cathode), (d) motorized stage, (e) fuel cell test station, (f) temperature controllers

3.2.4. Material Properties of Cell Components

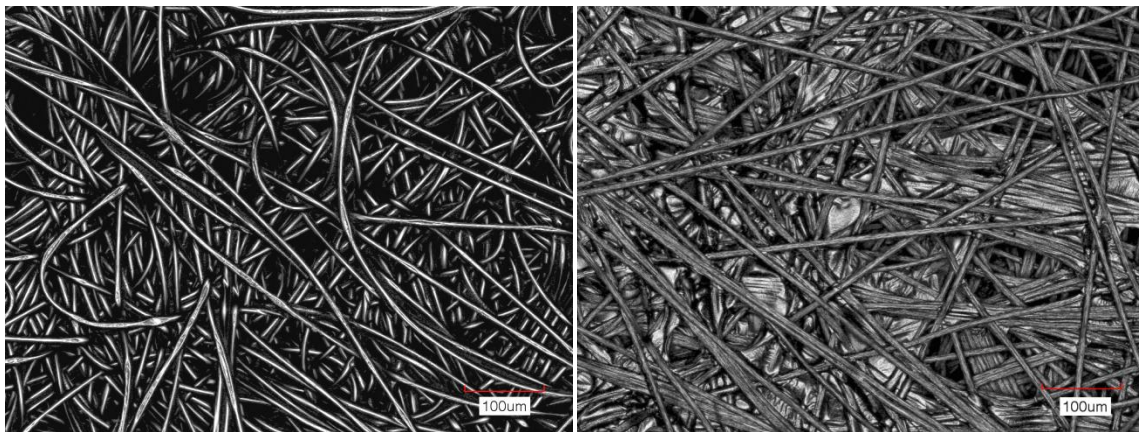
Two different commercially available carbon paper gas diffusion layer samples were used for this testing: Freudenberg H2315 and Toray TGP-H-060, both coated with an in-house microporous layer (MPL) by General Motors. The properties of the two GDL samples are summarized in Table 3.2. Confocal laser scanning microscope images of the GDL samples are shown in Figure 3.7. The W.L. Gore Inc. catalyst coated membrane used in these experiments was fabricated on an 18 μm thick perfluorosulfonic acid (PFSA) membrane and has a platinum loading of 0.2/0.3 (an/ca) $\text{mg Pt}/\text{cm}^2$. The contact angles of the gold plated current collectors and Lexan windows are approximately 85° and 60° , respectively.

Table 3.2 - GDL material properties.

Property	Freudenberg H2315	Toray TGP-H-060
Type	Air-laid hydro-entangled carbon fiber paper	Wet-laid carbon fiber paper
Thickness* (μm)	210	190
Contact Angle ($^{\circ}$)	153	150
MPL Coating**	Yes	Yes

*Value reported by manufacturer

**In-house MPL by General Motors



(a)

(b)

Figure 3.7 - Confocal laser scanning microscope images of (a) Freudenberg H2315 GDL and (b) Toray TGP-H-060 GDL.

3.3. Experimental Procedure

3.3.1. Fuel Cell Operating Conditions

The experiments described in this section were performed with a cell temperature of 35 °C and fully humidified inlet gases (100 %RH). As indicated by Owejan et al. [5], conditions of low temperature, low power and low stoichiometric ratio are especially susceptible to an accumulation of liquid water within the flow field channels and GDL, and can represent a considerable portion of the cell's operational lifetime. Therefore, an analysis of two-phase flow occurring in the gas channels under these operating conditions can provide valuable

insight towards water mitigation strategies at these inevitable operating conditions. A summary of the experimental parameters are shown in Table 3.3.

Table 3.3 - Fuel cell parameters for optical visualization experiments.

Parameter	Value
Active Area	50 cm ²
Membrane Thickness	18 μm
Catalyst Loading	0.2/0.3 (an/ca) mg Pt/cm ²
Anode Fuel	Hydrogen
Cathode Oxidant	Air
Cell Temperature	35 °C
Inlet Humidification	100%/100%
Stoichiometric Ratios (an/ca)	1.5/2.5, 1.5/5, 3/8

3.3.2. Fuel Cell Testing Procedure

Prior to running a test, dry reference videos of each viewing window were recorded. The fuel cell was then subjected to conditioning with fully humidified gases and operation at ~0.60 V. After the cell was conditioned, the load was removed from the cell so it could stabilize at open circuit voltage (OCV). After the cell voltage stabilized it was kept at OCV for 10 minutes to allow steady state to be reached. A point was then added to the polarization curve and the load was increased. For each test, current density was increased in increments of 50 mA/cm² from 50 mA/cm² to 400 mA/cm², and in increments of 100 mA/cm² for each additional test point until cell failure. At each load point, prior to recording any data, the cell operated for 10 minutes in order to achieve steady state voltage and water production (an additional 5 minutes was added for lower current densities if steady state water had not been reached, as determined by visual observation). Data was recorded starting with the fourth (top) window and moving downwards to the first (bottom) window. This was due to the increased water production along the length of the cell as the reactant gases are consumed,

thus the windows closer to the cell inlets reach steady state water production more rapidly. For each window, simultaneous anode and cathode videos were recorded. In addition to videos, visual observations of two-phase flow patterns present in the windows were manually recorded. Once data and videos had been recorded for each window, a point was added to the polarization curve, an HFR reading was taken, and the load to the cell was incremented.

3.3.3. Data Acquisition and Processing

In order to fully characterize the cell during operation, polarization curves were recorded for cell performance and HFR measurements were recorded for the membrane hydration state. The polarization curves were recorded using the Hydrogenics test station, and the cell voltage at each current density was plotted using a built in graphical function and monitored during operation. After each test, the data was saved and exported so it could be plotted externally from the test station. HFR values were also taken from the test station by applying a ripple current of 10 amps at operating conditions where the current density was 100 mA/cm² or higher, and recording the associated resistance at steady state.

3.3.4. Video Recording Procedure

Videos of two-phase flow in the anode and cathode gas channels were recorded using Photron FASTCAM Viewer version 3.2. This software allows for two high speed cameras to be controlled and viewed simultaneously, as shown in Figure 3.8 with the anode facing camera feed displayed on the left and the cathode facing camera feed on the right.

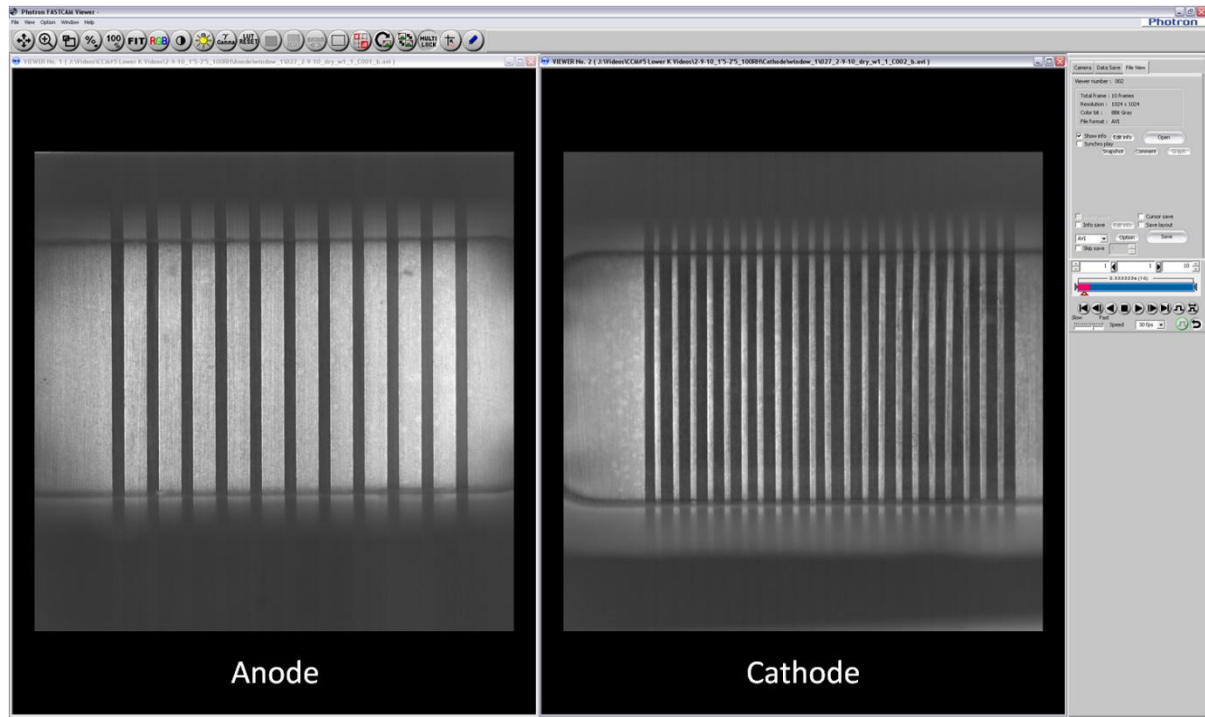


Figure 3.8 – Photron Fastcam Software used for simultaneous visualization of anode (left) and cathode (right) flow channels.

The videos were recorded at a frame rate of 60 frames per second and a shutter speed of 1/60 s. The trigger was set to center mode which records the content directly before and after when the trigger is input. This mitigated any delays between visual observation and triggering of the video recording when dynamic two-phase flow was present. For each operating condition, the cell was allowed to reach steady state as described in Section 3.3.2., with videos of each window recorded starting with the fourth (top) window and incrementing down to the first (bottom) window. The window closest to the inlet manifold was not observed due to visual interference from individual channel pressure tubing.

Each window was observed and videos were recorded when any two-phase flow events were taking place, such as dynamic film and slug transport in the channels, in order to capture representative maximum water content present at steady state operation at each condition. In many cases, multiple videos were recorded of the same window in order to obtain an average steady state maximum water level. If no significant dynamic two-phase events were occurring, or if there was not a significant amount of two-phase flow present, a single video was recorded to document the steady state water content.

4. Digital Video Processing Methodology

4.1. Overview

In order to obtain information about the liquid water present in the flow field channels during cell operation, a video processing algorithm was developed. Video processing is a powerful tool that can be used to extract information from a sequence of images. The goal of the developed algorithm was to automatically detect and isolate dynamic and static liquid water in the fuel cell channels and quantify it as a ratio of the liquid water area in the channels to the total flow field channel area. The video processing algorithm was developed and written in MATLAB, and utilized functions from the Image Processing Toolbox™. Each video was processed on a frame-by-frame basis, with the processed frames compiled back together in order to form a final processed video. Relevant quantification data was automatically extracted and saved. The algorithm utilized arithmetic operators and image segmentation techniques in combination with morphological processing to reveal key information about liquid water within the operating fuel cell. An additional algorithm was developed to automatically distinguish between the different flow structures present in the channels, and provide information about the distribution of liquid water among the flow structures.

4.2. Analysis of Digital Videos and Images

The dual-visualization setup described in Section 3.2.3. was used to simultaneously record digital videos of the anode and cathode flow fields during cell operation using Photron high speed cameras. Each digital video is comprised of a sequence of frames, or digital images. An image can be defined as a two-dimensional function, $f(x, y)$, where x and y are the spatial coordinates, and the amplitude of f at any coordinate pair represents the intensity at that location [32]. Each coordinate location is referred to as a picture element, or pixel. Digital images are often represented as a multidimensional matrix or array populated with the intensity values of each pixel. When considering the digital video as a whole, it can be considered a three-dimensional function, $f(x, y, t)$, with time, t , as the third dimension. Since the images/videos captured in this study are digital, the values of x , y , f , and t are finite and discrete. A representation of a digital image and video are shown in Figure 4.1. The digital video frames recorded using the Photron high speed cameras in the dual-visualization setup are intensity (grayscale) images. An intensity image contains only shades of gray, ranging

from black at the lowest intensity to white at the highest intensity. Another type of image used in this work is a binary image, which is a logical array containing only two possible pixel values: white pixels with a value of 1 (foreground objects) and black pixels with a value of 0 (background).

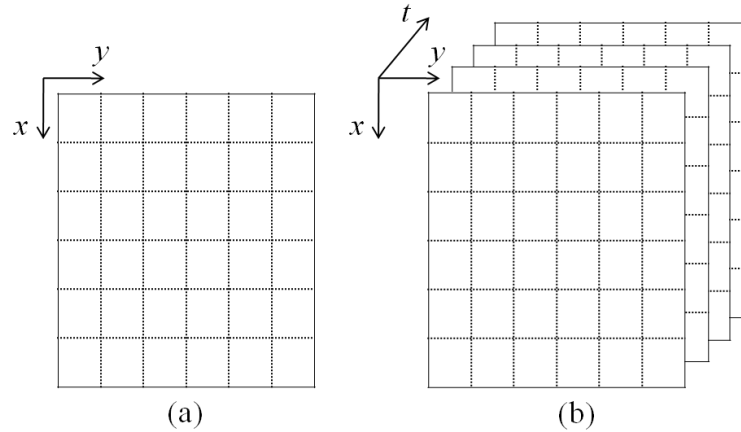


Figure 4.1 - Representation of (a) digital image, and (b) digital video. The dotted squares represent the picture elements (pixels) of the image.

When performing image processing operations it is necessary to consider the data class of the image. There are several different data classes, but only three were utilized in this work: unsigned 8-bit, double precision, and logical. A summary of these three data classes is provided in Table 4.1. The digital video frames recorded using the Photron cameras are unsigned 8-bit images. In MATLAB, all numeric computations are performed using double precision [33]; therefore, conversions between classes (especially between double precision and unsigned 8-bit) were often necessary when performing the image processing operations in MATLAB.

Table 4.1 - Summary of data classes.

Data Class	Values	Range
Unsigned 8-bit (uint8)	Unsigned Integers	0 to 255
Double Precision (double)	Floating-Point Numbers	-10^{308} to 10^{308}
Logical	True or False	1 (true) or 0 (false)

There are two different kinds of arithmetic operations in MATLAB: matrix arithmetic operations, which follow the conventional rules of linear algebra, and array arithmetic operations, which are performed on an element by element (or pixel by pixel) basis. Most of the arithmetic operations performed in this work are array operations since they are suitable for use with multidimensional arrays.

4.3. Theory of Morphological Image Processing

Morphological processing is an image processing technique based on the principles of mathematical morphology. Mathematical morphology is a theory for the analysis of spatial structures and is based on set theory, integral geometry, and lattice algebra [34]. In this work, morphological processing is performed on the thresholded binary frames (as described later in Section 4.4.4.) in order to further isolate and extract the pixels representing static and dynamic liquid water present in the fuel cell gas channels during operation.

In morphological theory, a binary image is considered to be the set of its foreground pixels (white pixels with a value of 1), the elements of which are in the 2-D integer space, \mathbb{Z}^2 [32]. A structuring element (SE) is a pre-defined shape which is a subset of \mathbb{Z}^2 . The basis of morphological processing is the use of structuring elements to ‘probe’ an image and determine where the SE does or does not fit within the binary image, and then use these locations to derive structural information about the image [35]. Some of the more commonly used structuring elements are a cross, square, or disk as depicted in Figure 4.2.

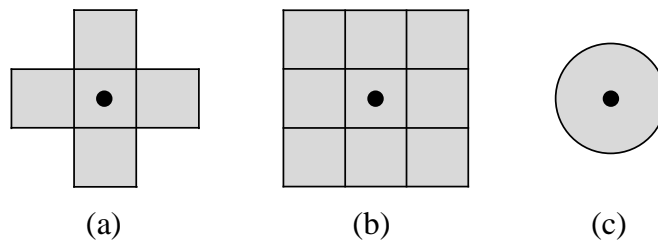


Figure 4.2 - Common structuring elements (SEs) used in morphological processing: (a) cross, (b) square, and (c) disk. The black dots represent the origin of the SEs.

The morphological operations of opening and closing are utilized within this algorithm to isolate the liquid water pixels. In order to understand these operations, it is necessary to understand erosion and dilation, which are the two fundamental morphological operations

upon which many morphological algorithms, including opening and closing, are based. Erosion is a shrinking or thinning operation, where the extent of shrinking is controlled by the nature of the structuring element. With A and B being sets in \mathbb{Z}^2 , the mathematical definition of the erosion of A by B , denoted $A \ominus B$ in Equation (4.1), is

$$A \ominus B = \{z | (B)_z \subseteq A\} \quad (4.1)$$

where B is the structuring element, z is a set of all points in \mathbb{Z}^2 , and $(B)_z$ represents the translation of B by z [32]. That is, the erosion of A by B is the set of all points z such that B is a subset of A when its origin is located at z . The erosion operation represents filtering on the inside of an object, and is useful for eliminating small extrusions. Figure 4.3 shows an example erosion operation.

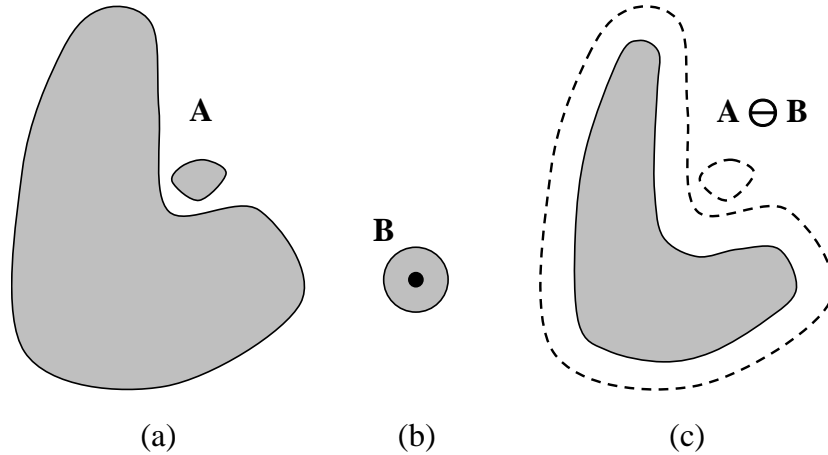


Figure 4.3 - Erosion operation: (a) set A, (b), structuring element B, (c) erosion of A by B, with dotted line representing original set A.

Dilation is a growing or thickening operation, where the extent of the thickening is controlled by the nature of the structuring element. With A and B being sets in \mathbb{Z}^2 , the mathematical definition of the dilation of A by B , denoted $A \oplus B$ in Equation (4.2), is

$$A \oplus B = \{z | [(\hat{B})_z \cap A] \subseteq A\} \quad (4.2)$$

where B is the structuring element, and the operation is based on reflecting B about its origin and then shifting this reflection, \hat{B} , by the set of points z [32]. The dilation of A by B is thus considered the set of all points such that the reflected and translated B overlaps A by at least

one element when its origin is located at z . The dilation operation represents filtering on the outside of an object, and is useful for filling in small extrusions. Figure 4.4 shows an example dilation operation.

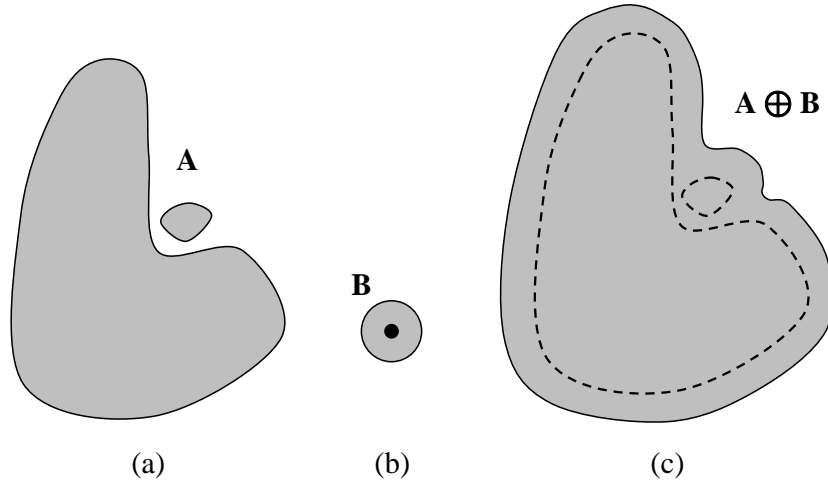


Figure 4.4 - Dilation operation: (a) set A, (b) structuring element B, (c) dilation of A by B with dotted line representing original set A.

Opening and closing, which were used in the video processing algorithm developed in this work, are secondary morphological operations based upon erosion and dilation. Opening is used on an object to smooth its contour, break narrow connections, and eliminate thin protrusions, while closing is used to join narrow breaks, eliminate small holes, and fill gaps in the object's contour [32]. A morphological opening is an erosion followed by a dilation, denoted in Equation (4.3) as

$$A \circ B = (A \ominus B) \oplus B \quad (4.3)$$

where A is the binary image and B is the structuring element. Contrary to the opening operation, closing is a dilation followed by an erosion, denoted in Equation (4.4) as

$$A \bullet B = (A \oplus B) \ominus B \quad (4.4)$$

where A is the binary image and B is the structuring element. Opening and closing have opposite behaviors; opening removes the object pixels which are not covered by the translations of the structuring elements that fit the image objects, while closing adds the background pixels which are not covered by the translations of the structuring element that fit

the image background [34]. An example comparing of opening and closing operations is shown in Figure 4.5.

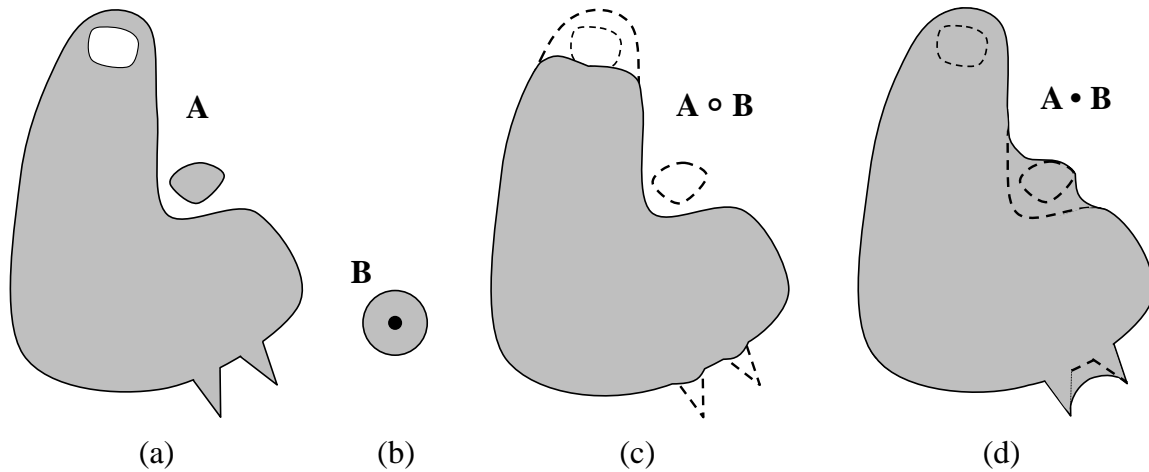


Figure 4.5 - Comparison of opening and closing operations: (a) set A, (b), structuring element B, (c) opening of A by B with dotted line representing original set A (d) closing of A by B with dotted line representing original set A.

A specific type of morphological opening called area opening filters an image by removing connected components whose area (which is defined by number of pixels) is smaller than a specified value [34], and is expressed in Equation (4.5)

$$A \circ (\alpha)_E = \cup \{C_i | \text{area } C_i \geq \alpha\} \quad (4.5)$$

where A is the binary image, α is the specified area, E is the connectivity of α , and C_i is the connected components in A [35].

Connected components are sets of pixels within a binary image whose pixels possess a certain spatial proximity. The spatial relationship between individual pixels is defined in terms of neighbors; pixels which are vertically or horizontally adjacent are 4-neighbors, and pixels which are either 4-neighbors or diagonally adjacent are 8-neighbors, as depicted in Figure 4.6. A group of pixels is 4- or 8-connected if for two foreground (object) pixels, there exists a path of foreground pixels between them where each pixel in the path is a 4- or 8-neighbor of the next, respectively. The sets of these connected foreground pixels are referred to as connected components.

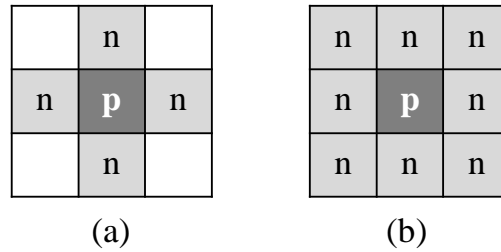


Figure 4.6 - Pixel neighborhoods: (a) pixel p and its 4-neighbors, n, (b) pixel p and its 8-neighbors, n.

Other morphological processing operations performed in this algorithm are bridging and filling, which are built into the MATLAB Image Processing Toolbox. The bridge function connects pixels which are separated by a single pixel gap by changing a pixel's value from 0 to 1 if it has two non-zero neighbors which are not connected. The filling function is used to fill holes in objects, where a hole in a binary image is defined as a set of background (0-valued) pixels that cannot be reached by filling in the background from the edge of the image. Hole filling changes the value of the pixels in these sets from 0 to 1.

4.4. Video Processing Algorithm

4.4.1. Input Files

The inputs required for the video processing algorithm are a dry reference video, a test video, and an image mask. The dry reference videos are taken of each window prior to testing, when no two-phase flow is present in the channels. The test videos are taken of each window during cell operation and capture any two-phase flow that is present at steady state for each current density. The image mask is a logical image whose pixel values are 1 in the region of interest, and 0 everywhere else. Performing array multiplication of an image by a mask changes pixels in the image that are not in the region of interest to 0, while leaving the pixels in the region of interest unchanged. In this work, the masking operation changes the land area pixel values to 0, leaving only the channel regions for analysis. Figure 4.7 illustrates a masking operation, and a sample dry image and its corresponding mask image are shown in Figure 4.8.

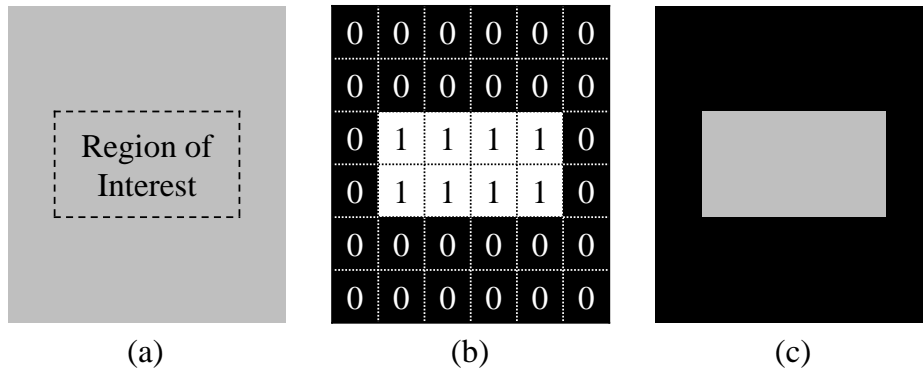


Figure 4.7 - Masking operation: (a) original image containing region of interest, (b) image mask, (c) array product of (a) and (b).

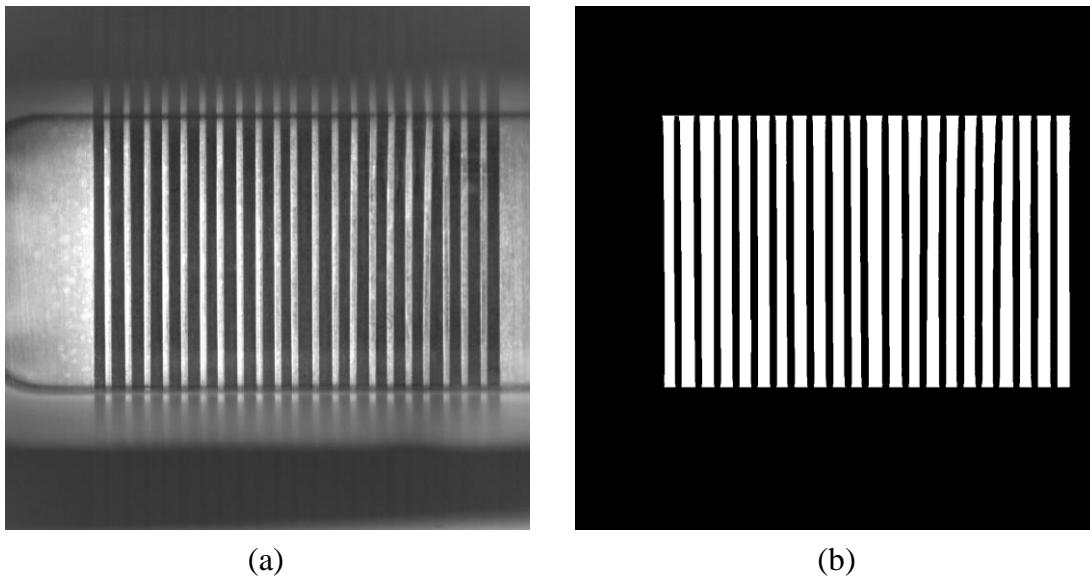


Figure 4.8 - (a) Dry video frame, cathode window #1, (b) corresponding mask image, with white pixels representing channel area.

4.4.2. Pre-Processing

Prior to detecting liquid water in the test video frames, it was necessary to perform a series of pre-processing steps. In order to reduce any noise present in the frames, the dry video frames are averaged to a single frame. First the dry video frames are read into MATLAB as unsigned 8-bit intensity images and converted to double precision images so that numeric computations can be performed on the images. A for loop is then used to add each subsequent frame of the dry reference video to the sum of the previous frames, and the final

summed frame is then divided by the total number of frames in the video, resulting in an averaged frame, as shown in Equation (4.6)

$$\frac{1}{N} \sum_{t=1}^N D_t \quad (4.6)$$

where N is the total number of frames in the video, t is the frame number (time), and D is the dry video.

The intensity of the average dry frame is scaled by dividing the frame by its mean intensity in order to account for any uniform variations in illumination that may have occurred while capturing the videos. Following this step, the dry frame is multiplied by the mask image, revealing only the channel regions for analysis. Likewise, after being read into MATLAB, each frame of the test video is converted to double precision image, the intensity is scaled, and the frame is multiplied by the mask image.

4.4.3. Image Subtraction and Segmentation

Once the pre-processing steps have been performed on the dry and test videos, the differences in pixel intensities between the averaged dry reference frame and the test video frames are used to reveal the locations in which liquid water is residing in the channels. A for loop was implemented such that the absolute difference is taken between the dry reference frame and each subsequent frame in the test video as shown by Equation (4.7),

$$P_{i,j,t} = |W_{i,j,t} - D_{i,j}| \quad \forall i, j, t \in W \quad (4.7)$$

where P is the processed video, W is the test video, D is the dry reference frame, and i, j , and t are the row, column, and time (frame number) respectively. For each frame of the test video, once the difference image has been computed, the pixel intensity values are divided by the maximum intensity value for that image. This ensures that when the difference image is saved as an unsigned 8-bit image for analysis, the intensity values will not be ‘clipped’ if they are outside the range of 0 to 1. A sample difference image is shown in Figure 4.9. The digital counts of the difference image are scaled so that it is visible.

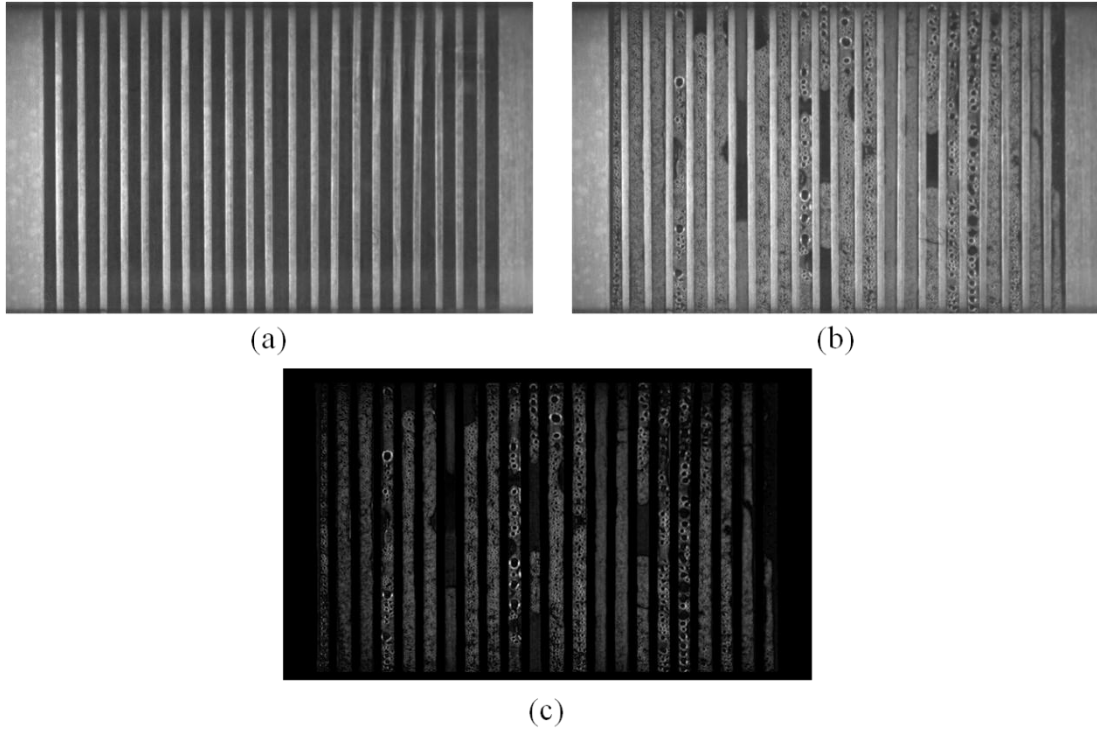


Figure 4.9 - Sample images from cathode window #1: (a) dry video frame, (b) test video frame, (c) resulting absolute difference image of (a) and (b).

Once the difference image has been obtained, image segmentation is used to extract the pixels representing liquid water in the channels based on their intensity. Image segmentation is a technique used to subdivide an image into its constituent regions or objects; the segmentation of non-trivial images is considered to be one of the most difficult tasks in image processing [32]. Region-based image segmentation is the process of separating an image into similar regions based on predefined criteria, such as pixel intensity. One of the most commonly used region-based segmentation applications is thresholding [32]. Thresholding categorizes pixels as either ‘foreground’ pixels (objects) or ‘background’ pixels, based on their value relative to a specified intensity, or threshold value. Typically, pixels with intensity greater than the selected threshold value are assigned the value of 1, and considered to be foreground pixels, whereas pixels whose intensity is less than the threshold value are considered to be background pixels and assigned a value of 0. As described by Gonzalez and Woods [32], the thresholded image is defined in Equation (4.8) as

$$g(x, y) = \begin{cases} 1 & \text{if } f(x, y) \geq T \\ 0 & \text{if } f(x, y) < T \end{cases} \quad (4.8)$$

where $g(x, y)$ is the thresholded frame, $f(x, y)$ is the original frame, and T is the threshold value. Thus, the resulting thresholded image is a binary image, or logical array, containing only foreground and background pixels with values of 1 and 0, respectively.

The thresholding of the difference image in this algorithm is a critical step towards the successful detection of liquid water in the fuel cell channels. In addition to the static and dynamic liquid water present in the channels, a significant amount of condensation is usually present in the channels as a result of the humidified inlet gases. As a result, there are generally three intensity ranges present in the difference image: (1) intensity values representing ‘unchanged’ channel area, where no liquid water or condensation is present, (2) intensity values representing locations where liquid water is present, and (3) intensity values corresponding to the presence of condensation. These regions are highlighted in Figure 4.10.

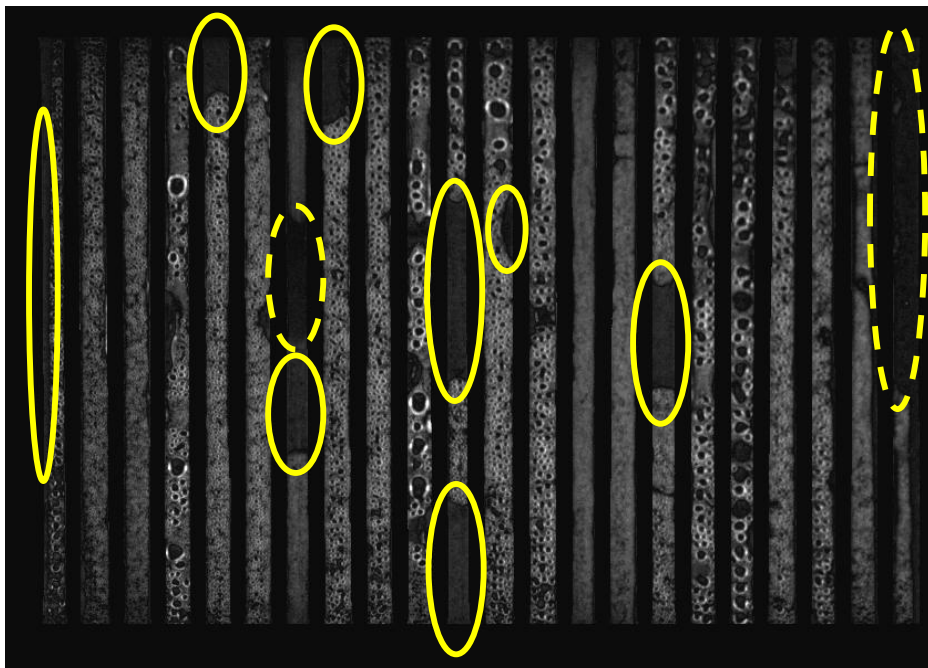


Figure 4.10 - Difference image from Figure 4.9(c) with different intensity regions highlighted. Dashed yellow outline indicates unchanged GDL, solid yellow outline indicates liquid water, and remaining non-zero intensity values represent condensation on channel surface.

Since the only intensity values of interest are those representing liquid water in the channels, it was necessary to implement multiple thresholding, i.e. thresholding simultaneously with more than one value, as represented by Equation (4.9)

$$g(x, y) = \begin{cases} 1 & \text{if } T_1 < f(x, y) < T_2 \\ 0 & \text{otherwise} \end{cases} \quad (4.9)$$

where $g(x, y)$ is the thresholded frame, $f(x, y)$ is the difference frame, and T_1 and T_2 are the lower and upper threshold values, respectively.

The determination of the threshold values can be done automatically through an algorithm, or manually through visual inspection. Automatic thresholding algorithms are useful in situations when there are distinct regions of intensity present in the image histogram, however, the intensity values for the three features seen in the difference image were not easily distinguishable. In addition, it was found that there were some variations in intensity values for each of the viewing windows, requiring the use of different threshold values. Therefore, manual determination of threshold values was necessary in order to achieve more accurate results.

For each window, after calculating a difference image between a test video frame and the dry reference frame, the difference image was opened in an external image editing software, GIMP (GNU Image Manipulation Program). The threshold tool in GIMP enables the user to set a threshold range either by manually entering the upper and lower bounds or by using graphical sliders, and dynamic updating of the resulting thresholded image is displayed as the values are changed. This allows the user to easily identify the threshold values most suitable for isolating the pixels representing liquid water. To maximize the accuracy of threshold value selection, the original wet image is superimposed on top of the difference image and set to be semi-transparent so the pixels in the adjusted image can be visually correlated to the liquid water in the channels during thresholding. After an appropriate threshold range is selected for a particular window, the values are implemented into the algorithm for batch processing of videos. Since the threshold values are applied to the entire image, it is considered to be a global thresholding operation. A thresholded image from the difference image in Figure 4.10 is shown in Figure 4.11.

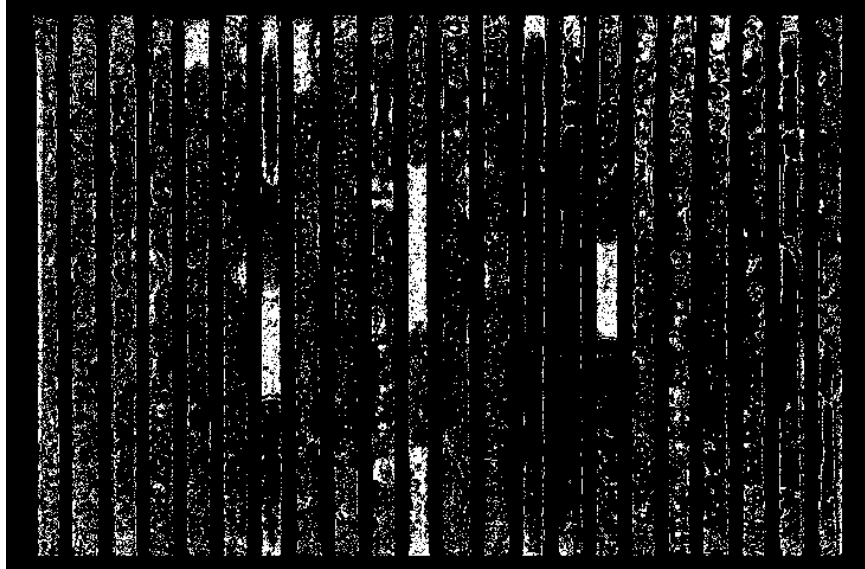


Figure 4.11 - Thresholded difference image. The locations with liquid water possess denser pixel regions.

As seen in Figure 4.11, because of the similarity of intensity values for the different features in the difference image, a ‘perfect’ segmentation is not possible using thresholding alone. Invariably, in addition to the liquid water pixels being isolated, some condensation pixels are also classified as objects. Some channel area where liquid water is not present may experience slight changes in pixel intensity due to lighting effects and can also be erroneously classified as objects. In order to refine the extraction of the liquid water objects in the channels, morphological processing is implemented on the thresholded images.

4.4.4. Application of Morphological Image Processing

The application of the morphological operations described in Section 4.3. allow for the complete isolation of liquid water pixels from the thresholded image. The first morphological processing technique applied to the thresholded frame is a hole filling, which increases the connectivity among the denser pixel regions, making them easier to extract. Figure 4.12 shows the thresholded image from Figure 4.11 with the holes filled in.

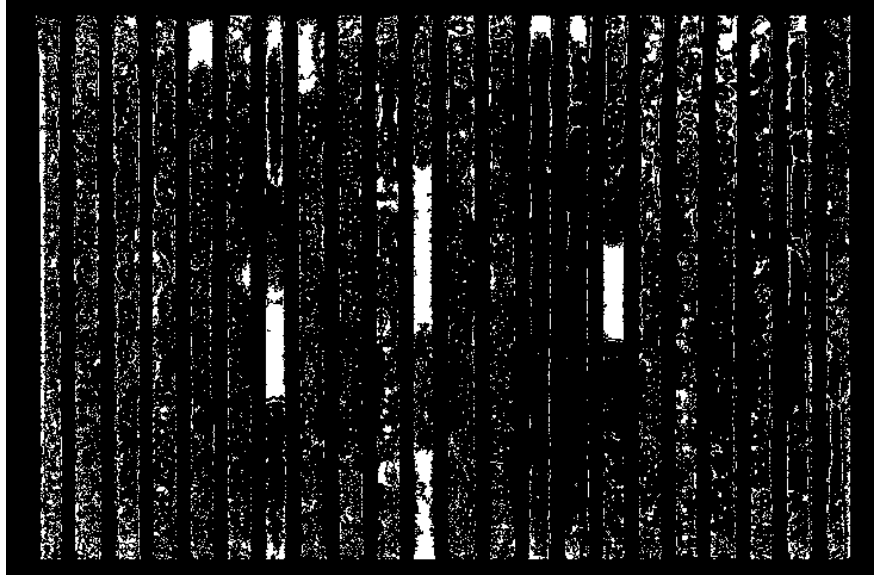


Figure 4.12 - Thresholded image after filling in holes.

An area opening filter is then applied to the image to remove irrelevant pixels representing condensation or noise, and the result is shown in Figure 4.13. The remaining connected components, which represent liquid water in the channels, typically experience some undesired reduction in area due to the opening, which must be recovered using additional morphological operations.



Figure 4.13 - Area opening of thresholded image. Remaining connected components represent liquid water in the channels.

In order to fill in some of the gaps in the pixel regions resulting from the area open filter, a bridging operation is performed followed by an additional hole filling, and the resulting image is shown in Figure 4.14.

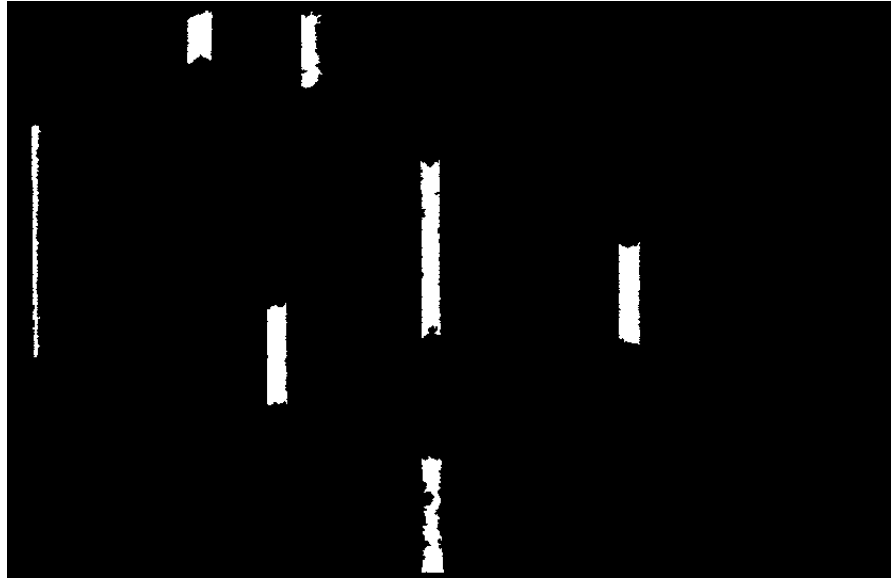


Figure 4.14 - Area opening image after hole filling and bridging operations.

The final morphological operation performed on the frame is a closing. This is done to further eliminate any remaining gaps in the contour of the objects. The structuring element used for the closing in the algorithm is a disk with a radius of eight. The resulting image is shown in Figure 4.15.



Figure 4.15 - Closing of Figure 4.14 using disk structuring element.

Following the completion of morphological processing, a faint representation of the original wet image is added to the processed frame for spatial context, as show in Figure 4.16. The processed frames are then converted back to unsigned 8-bit images and stitched back together sequentially to produce a final processed video. A flow chart of the entire video processing algorithm is presented in Figure 4.17, and the MATLAB code is presented in Section 9.1. (Appendix A).



Figure 4.16 - Final processed frame with faint reference frame added. Locations of liquid water in channels are represented by white pixels.

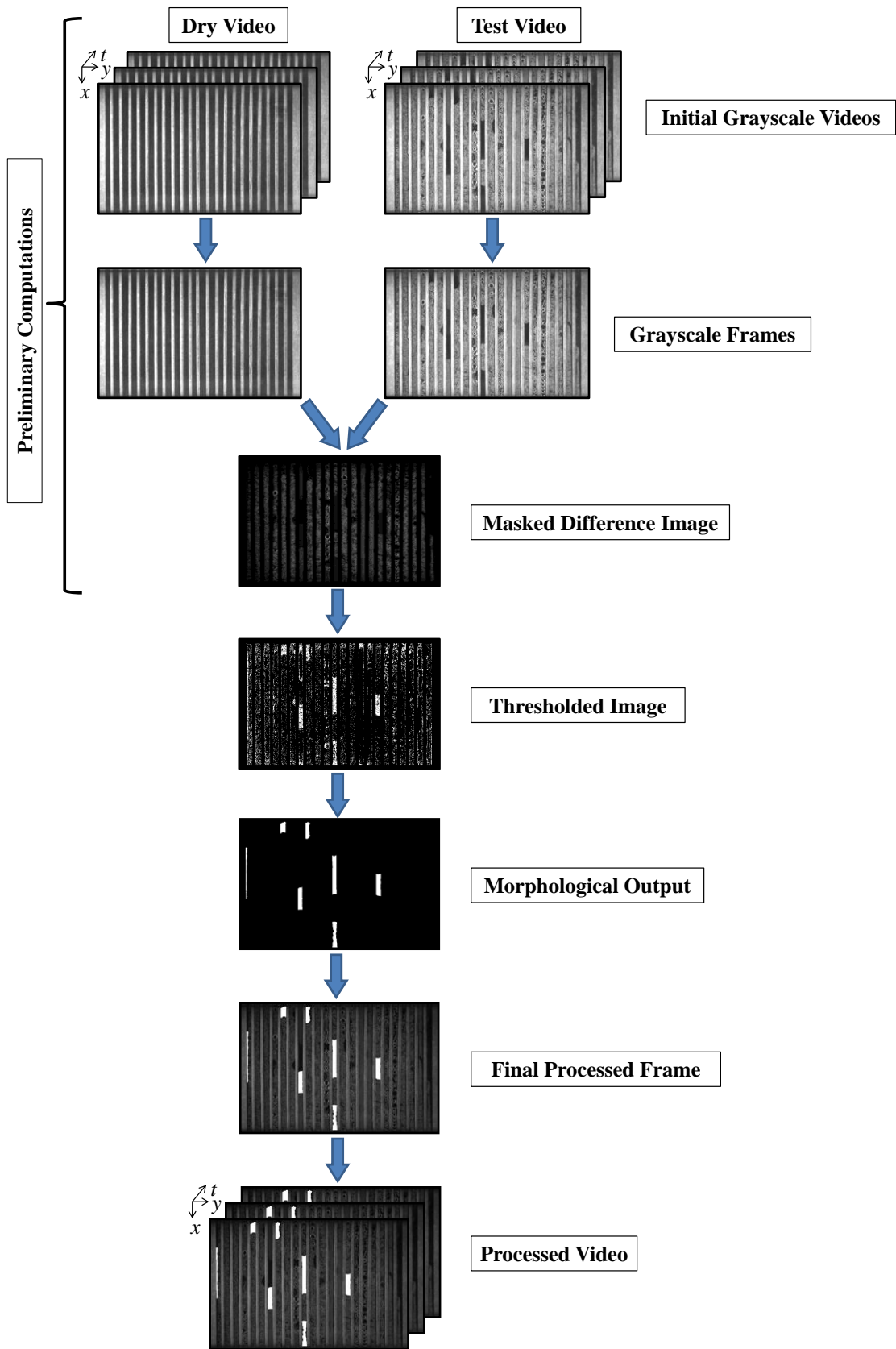


Figure 4.17 - Flow chart of video processing algorithm.

4.5. Calculation of Relevant Metrics

In conjunction with the processing of the individual frames, the algorithm was designed to automatically perform a series of calculations in order to obtain metrics relevant to the characterization and quantification of two-phase flow in the anode and cathode gas channels. The calculated metrics are presented in Table 4.2.

Table 4.2 - Metrics calculated by video processing algorithm.

Metric	Description	Calculation
Channel Pixels	Number of pixels representing the area in the channels	Count the number of channel (white) pixels present in the mask image
Channel Area	Total projected area of the flow field channels	Multiply the number of channel pixels by the dimension of a single pixel
Average Liquid Water Pixels	Average number of liquid water pixels present at steady state (max water) for a given operating condition and window	Mean value of water pixels for all frames of a processed video
Average Liquid Water Area	Average area of liquid water in the channels	Multiply the average liquid water pixels by the dimension of a single pixel
Water Coverage Ratio	Ratio of liquid water area to total projected channel area	Divide the average liquid water pixels by the channel pixels

4.6. Slug and Film Detection using Connected Components

Although the quantification of liquid water in fuel cell channels provides useful information, the ability to also discern the flow structure of the liquid water can greatly enhance the value of the quantification data. An additional algorithm was developed to assess the liquid water present in the test videos and automatically distinguish the flow structure of each liquid water object that was detected.

This algorithm used the anode and cathode test videos that had already been processed as described in Section 4.4. (without the addition of the faint reference frame) as inputs. The frames of these videos are binary images with detected liquid water objects represented by white pixels. For a given test video, each frame was labeled using a built in function of the Image Processing Toolbox. Labeling computes the connected components (objects) in a binary image based on a specified connectivity (4- or 8-connected). In the resulting label matrix, the pixels in each connected component are assigned consecutive integer values from 1 to the total amount of connected components in the frame. A representation of a binary image with connected components and the resulting label matrix are shown in Figure 4.18.

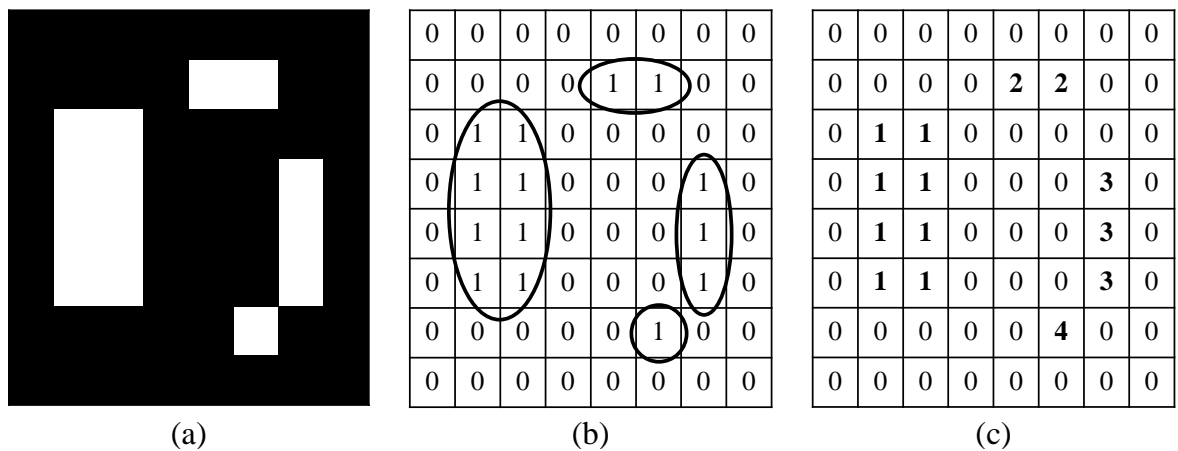


Figure 4.18 - Labeling of connected components in a binary image: (a) binary image, (b) corresponding pixel values of binary image, with 4-connected components highlighted, (c) resulting label matrix using 4-connectivity.

Once the label matrix was generated for a particular frame, it was added to its corresponding mask. This combined label matrix and mask image was then used for the flow structure characterization of each liquid water object. The pixel values of the mask image are 1 in the area of the channels and 0 everywhere else, and the label matrix pixel values are consecutive integers for each water object and 0 everywhere else. The resulting combined image had pixel values of 1 in the channel area not containing liquid water, each respective water object's integer value plus 1 for areas of liquid water inside the channels, and 0 in all other locations.

The algorithm developed in this work uses the pixel values surrounding each water object in the combined image to determine whether the object is a film or a slug, where a slug is defined as a water column that bridges the entire width of a channel. For each water object within a frame, the algorithm locates the indices of the object. It then finds the first row where the object is located, and then for that row it locates the first column where the object is located; these are the starting indices of that object. Beginning at this location, the algorithm checks the pixel value left, which can only be 0 or 1. If it is a 1, this means that the water object being evaluated is a film (in that particular row) because there is channel area to the left of it and thus it does not bridge the entire channel. Once an object is determined to be a film in a particular row, there is no need to evaluate that row further so the algorithm increments to the next row where the object is contained and finds the first column where the object is located in the new row and starts over. If the pixel value to the left of the starting indices is a 0, this means that the object could be a slug since it is contacting the channel wall on at least one side, and the algorithm then checks the value to the right. If the value to the right is the same as the starting pixel value (the object number integer plus 1) then it increments to the next column to the right and checks that pixel value. This continues until the value to the right is either a 0 or a 1. If it is a 1, the object is a film in that row, so the algorithm increments to the next row, finds the starting column for that row and starts the pixel value checking process over. If it is a 0, this means that the object is a slug since it contacts the channel wall on both sides. The object is then automatically classified as a slug, its area (in pixels) is recorded, and the algorithm moves to the next object and starts over. If every row of an object is checked without it being classified as a slug, it is classified as a film, its area is recorded and the algorithm moves to the next object and starts over. This process is repeated for each frame until all the water objects have been classified and their area recorded, at which point the algorithm increments to the next frame in the video and starts over with a new label matrix. A flow chart of this algorithm is shown in Figure 4.19, and the MATLAB code is presented in Section 9.2. (Appendix B). It was necessary to implement an algorithm to check each object on a row by row basis since there may be some inherent non-uniformity of channel width along the length of each channel due to the delicate nature of the flow fields.

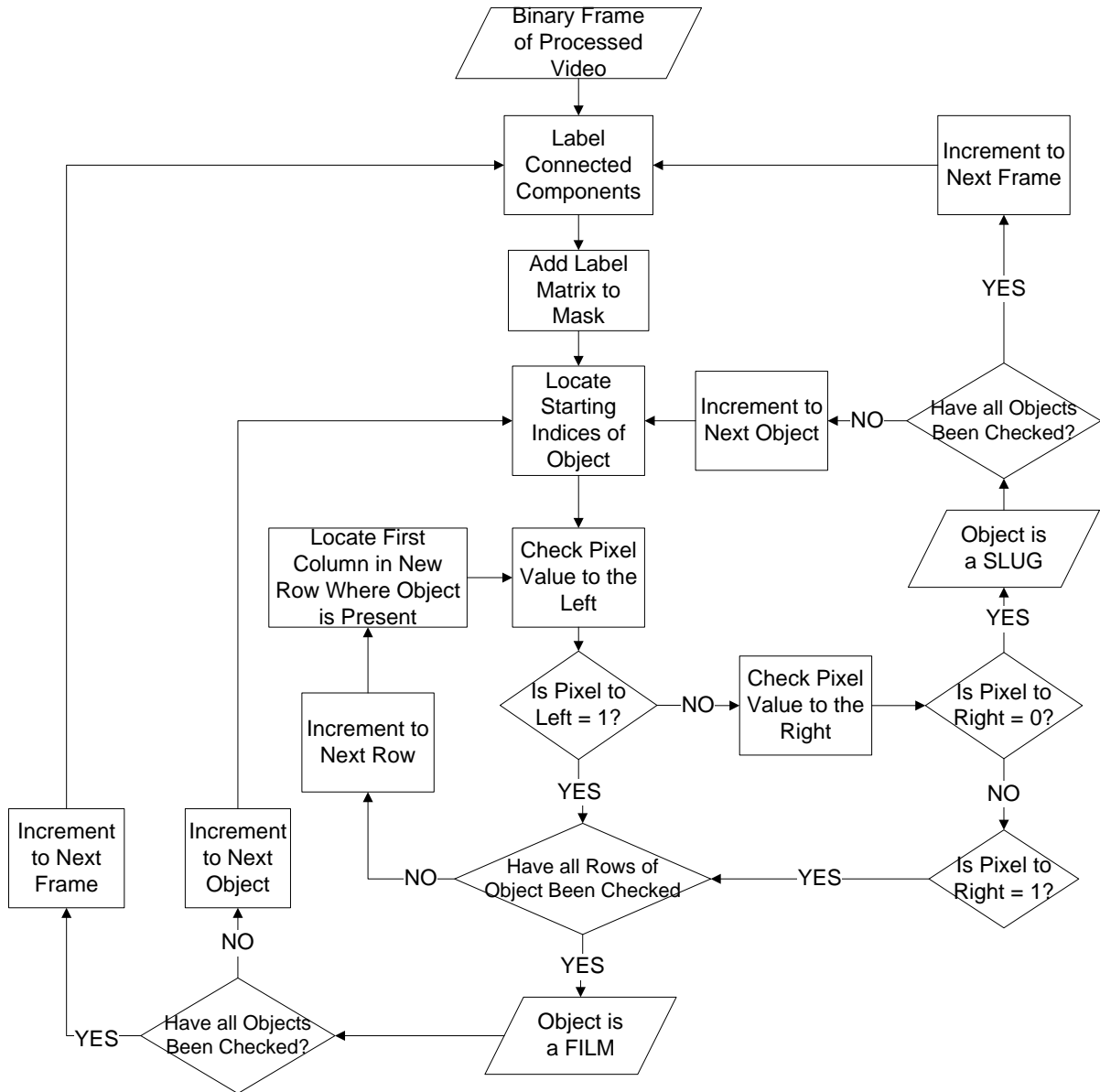


Figure 4.19 - Flow chart of slug/film detection algorithm, with the first frame of a processed test video as the starting input.

5. Results and Discussion

5.1. Fuel Cell Performance Characterization

The performance of the fuel cell with dual-visualization windows described in Section 3.2.2. was characterized using a Hydrogenics fuel cell test station. For each GDL sample at each stoichiometric ratio, a polarization curve was generated concurrently with the recording of test videos. In addition, HFR measurements were recorded to assess membrane hydration levels. Figure 5.1 shows the polarization curve and HFR for both GDL samples for a stoichiometric ratio of 1.5/2.5. The properties for the two GDL samples have been previously summarized in Table 3.2.

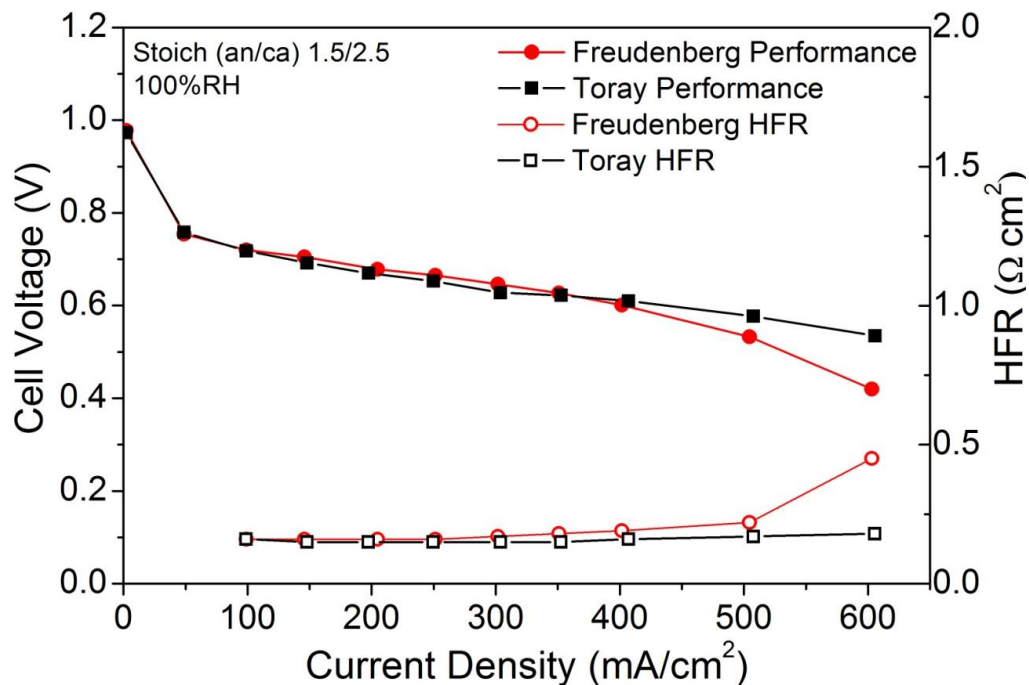


Figure 5.1 - Polarization curve and HFR for Freudenberg and Toray GDL samples.

Stoich (an/ca) 1.5/2.5, 100% RH inlet gases.

As seen in Figure 5.1, at a stoichiometric ratio of 1.5/2.5 and 100% RH, both GDL samples exhibited comparable performance at low and mid current densities. At higher current densities, the Freudenberg GDL performance decreased slightly compared to the Toray and showed a higher HFR measurement, indicating decreased membrane hydration. The same performance characterization was performed for stoichiometric ratios of 1.5/5 and 3/8 as shown in Figures 5.2 and 5.3, respectively.

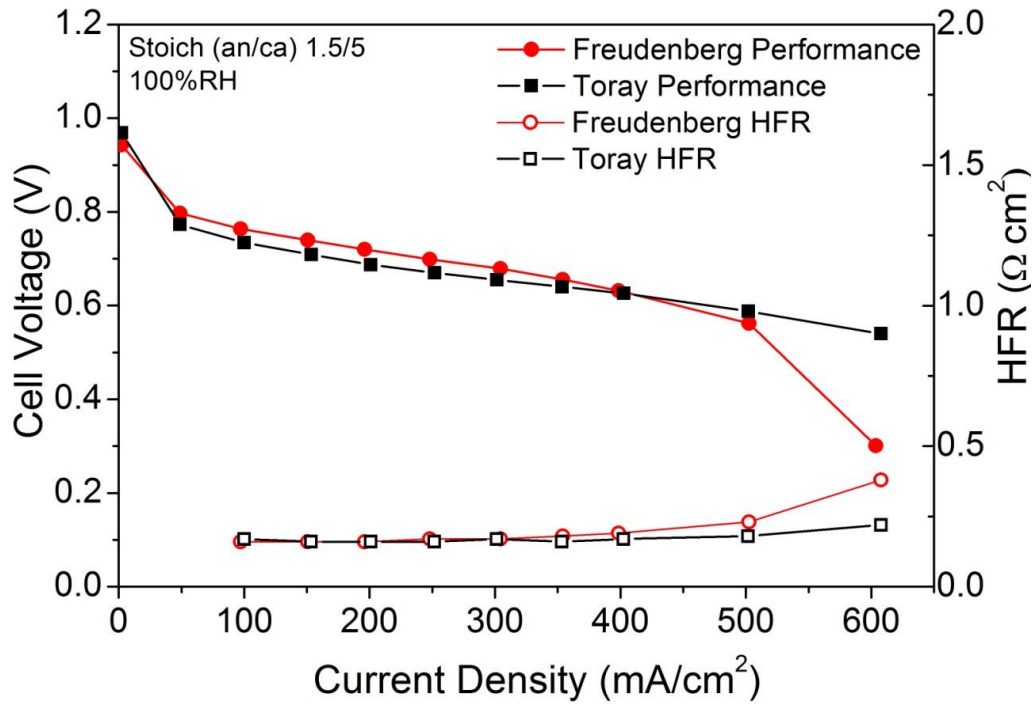


Figure 5.2 - Polarization curve and HFR for Freudenberg and Toray GDL samples.

Stoich (an/ca) 1.5/5, 100% RH inlet gases.

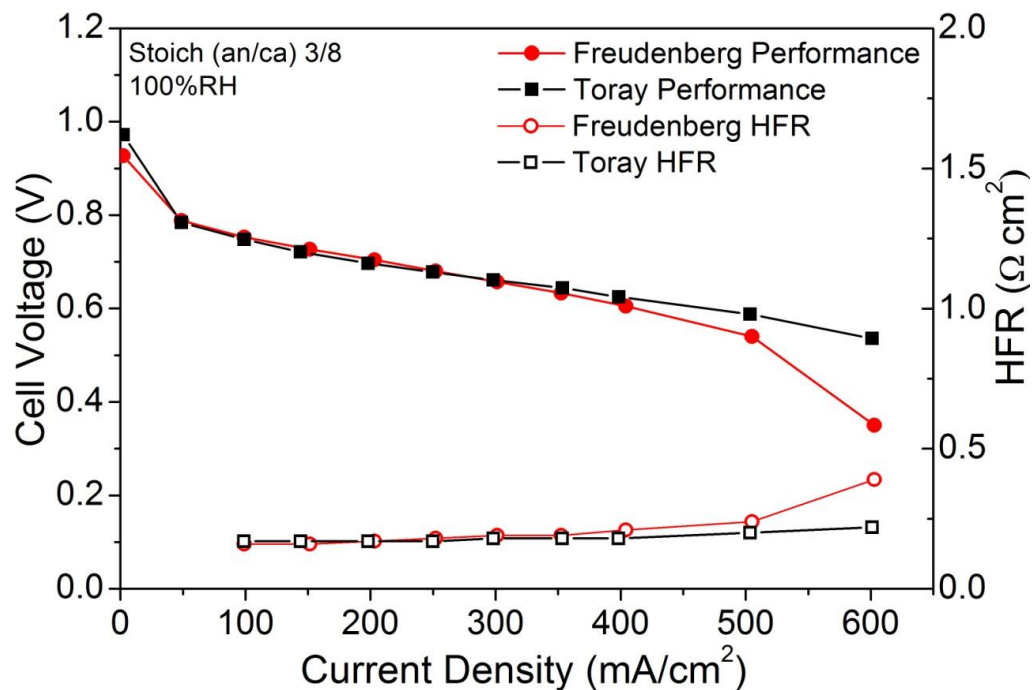


Figure 5.3 - Polarization curve and HFR for Freudenberg and Toray GDL samples.

Stoich (an/ca) 3/8, 100% RH inlet gases.

Similar performance results were observed for the 1.5/5 and 3/8 stoichiometric ratios, with both GDL samples exhibiting comparable polarization curves at the low and mid current densities, and with Toray maintaining higher performance and lower HFR at high current densities.

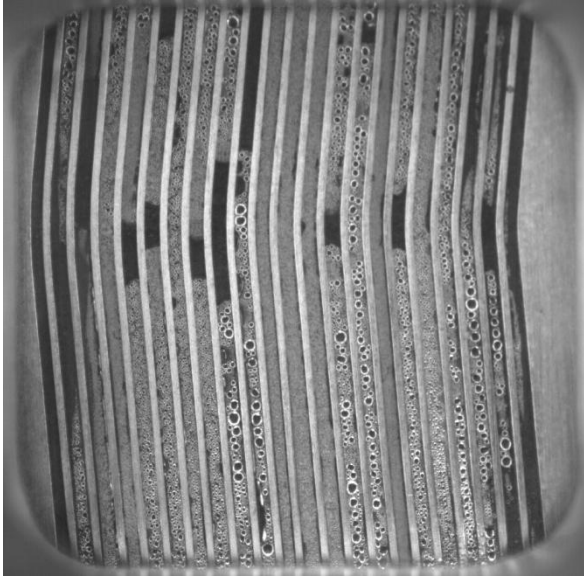
The overall low performance for the cell (compared to a standard fuel cell) is primarily due to the transparent materials on both the anode and cathode. The Lexan windows have an insulating effect and can cause internal cell temperature to increase significantly at higher current densities [6]. Since the Freudenberg GDL exhibits greater amounts of liquid water in the channels, the water is more readily removed from the cell at higher flow rates (higher current density). This, combined with the cell temperature effect, causes a rapid drying out of the Freudenberg cell at high current density, and thus the decaying polarization curve and HFR spike. The Toray GDL, however, does not display as much channel water but maintains a lower HFR value, indicating sufficient membrane hydration and implying a greater level of GDL saturation. The differences in flow field water content for both samples are discussed in detail in Sections 5.2. and 5.4.

5.2. Visual Observations of Two-Phase Flow in the Gas Channels

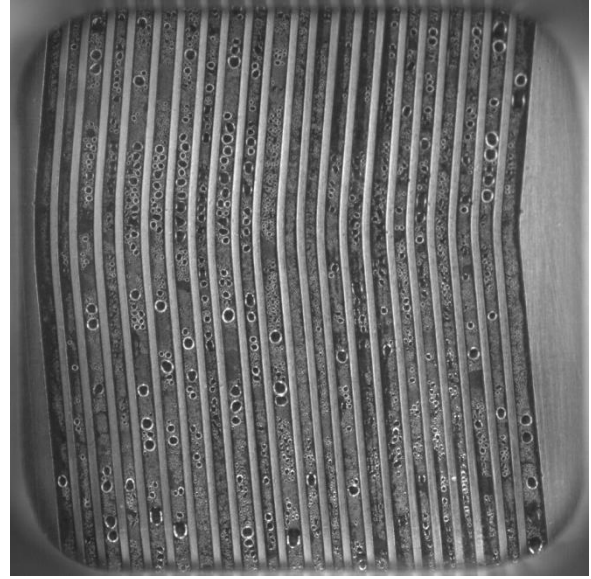
The dual-visualization setup described in Section 3.2.3. was used to simultaneously observe the anode and cathode flow fields, and record videos of the two-phase flow present in the gas channels during cell operation. Distinct differences in channel water content and dynamics were observed between the two GDL samples tested, and are described qualitatively in this section.

5.2.1. Stoichiometric Ratio 1.5/2.5

At a stoichiometric ratio of 1.5/2.5, the Freudenberg GDL sample exhibited a much greater presence of liquid water in the channels compared to the Toray sample. Both samples exhibited condensation on the Lexan window surface. On the cathode side, the presence of slug flow in the Freudenberg channels was more prominent in the low to mid current density range, whereas the Toray sample exhibited mostly small water films with minimum slug flow. At higher current densities, the Freudenberg flow field developed mist regions sooner, but still showed some active liquid water presence in the channels. Figures 5.4 – 5.6 show comparisons between the cathode flow fields for the two GDL samples.

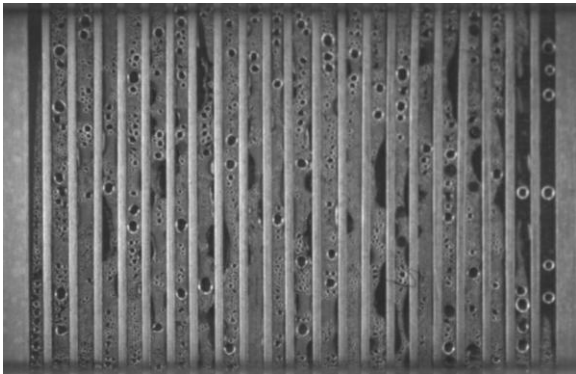


(a)

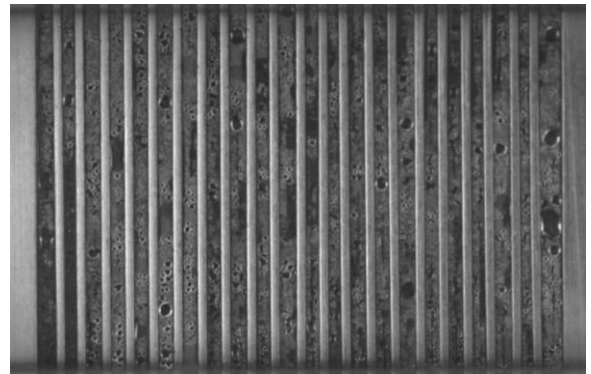


(b)

Figure 5.4 - Comparison of cathode window #2 for (a) Freudenberg and (b) Toray at stoichiometric ratio (an/ca) 1.5/2.5 and current density 100 mA/cm².

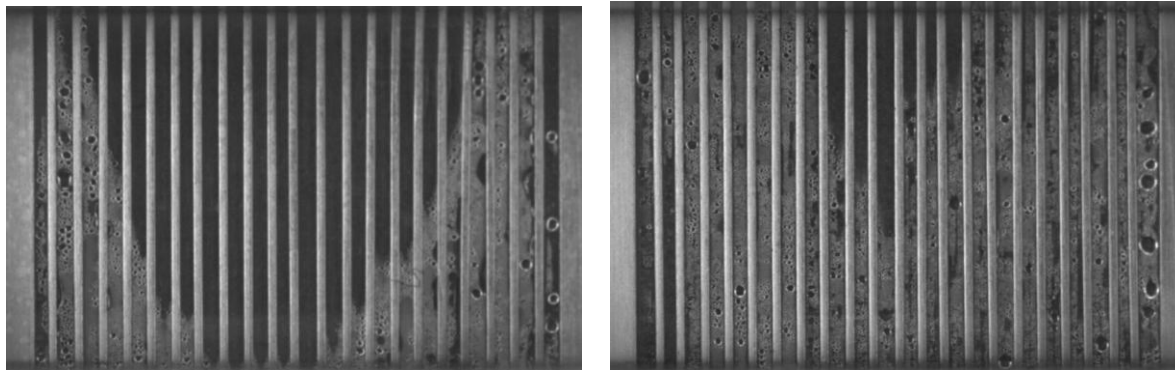


(a)



(b)

Figure 5.5 - Comparison of cathode window #1 for (a) Freudenberg and (b) Toray at stoichiometric ratio (an/ca) 1.5/2.5 and current density 300 mA/cm².

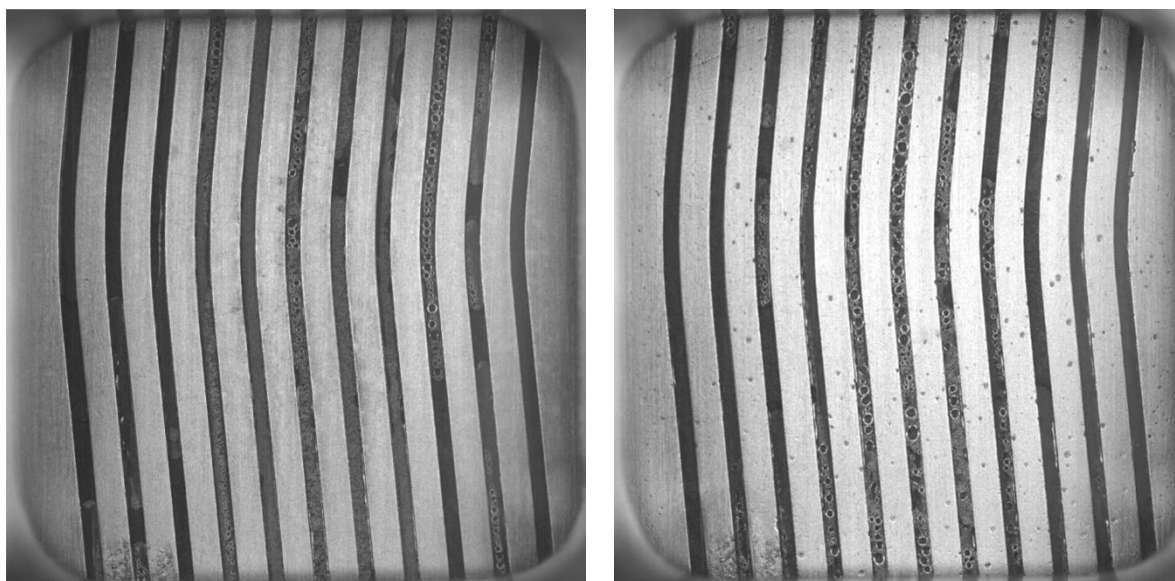


(a)

(b)

Figure 5.6 - Comparison of cathode window #1 for (a) Freudenberg and (b) Toray at stoichiometric ratio (an/ca) 1.5/2.5 and current density 500 mA/cm².

On the anode side of the cell, slug flow was dominant for both the Toray and Freudenberg GDLs for the low to mid current density range, and the Freudenberg channels maintained a greater amount of liquid water in the channels. The slug flow on the anode side was mostly static, and the low hydrogen flow rates posed difficulty in removing the liquid water from the channels. Figure 5.7 shows a comparison between the anode flow fields for the two GDL samples.



(a)

(b)

Figure 5.7 - Comparison of anode window #2 for (a) Freudenberg and (b) Toray at stoichiometric ratio (an/ca) 1.5/2.5 and current density 200 mA/cm².

5.2.2. Stoichiometric Ratio 1.5/5

The increased cathode flow rates lead to a significant decrease in the overall liquid water content in the anode and cathode channels for both GDL samples. There was also an increased presence of cathode film flow for the Freudenberg sample, compared to the lower stoichiometric ratio. On the anode side, slug flow still remained dominant for the Freudenberg GDL, while the Toray GDL showed a slight increase in film presence compared to the lower stoichiometric ratio. Figures 5.8 and 5.9 show images of the cathode and anode flow fields for each GDL sample.

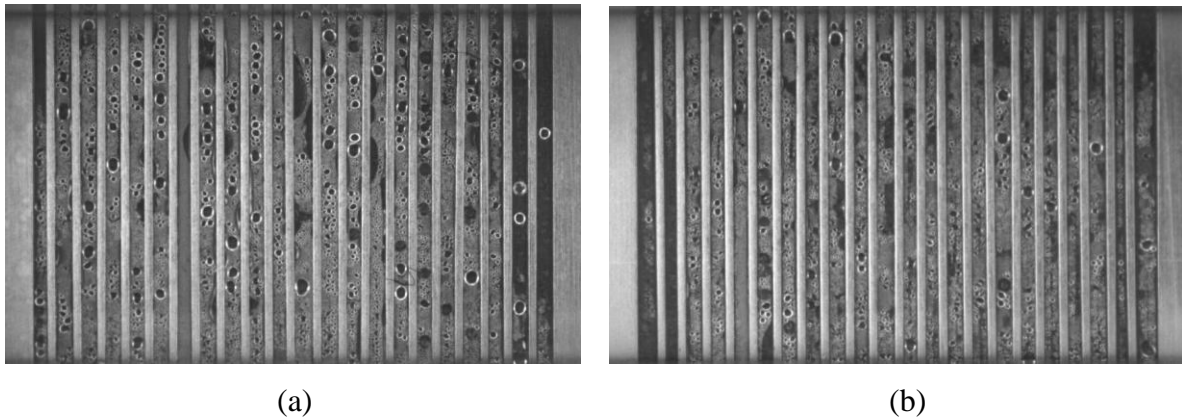


Figure 5.8 - Comparison of cathode window #1 for (a) Freudenberg and (b) Toray at stoichiometric ratio (an/ca) 1.5/5 and current density 150 mA/cm².

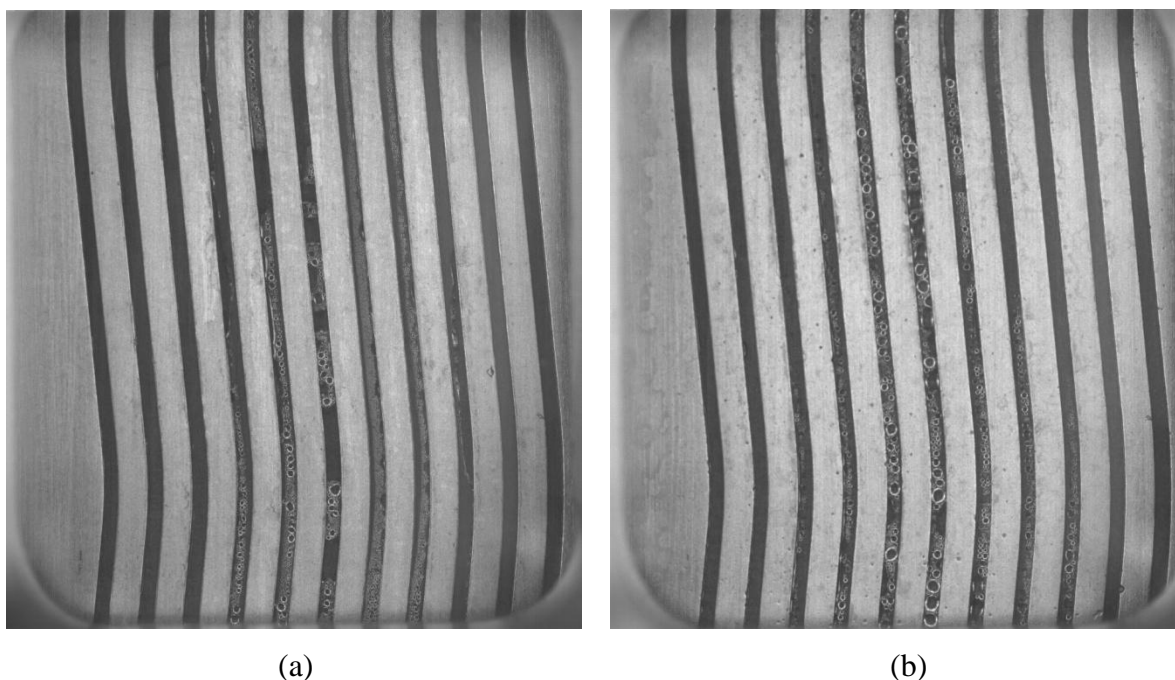
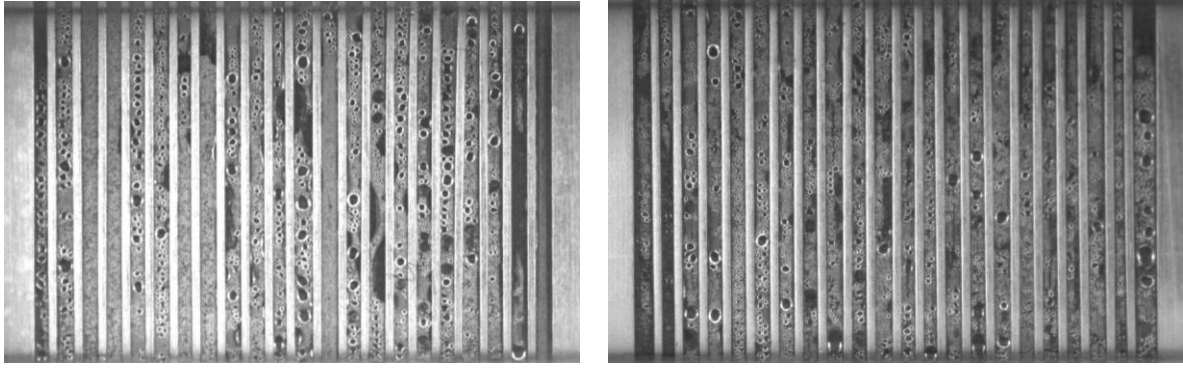


Figure 5.9 - Comparison of anode window #2 for (a) Freudenberg and (b) Toray at stoichiometric ratio (an/ca) 1.5/5 and current density 100 mA/cm².

5.2.3. Stoichiometric Ratio 3/8

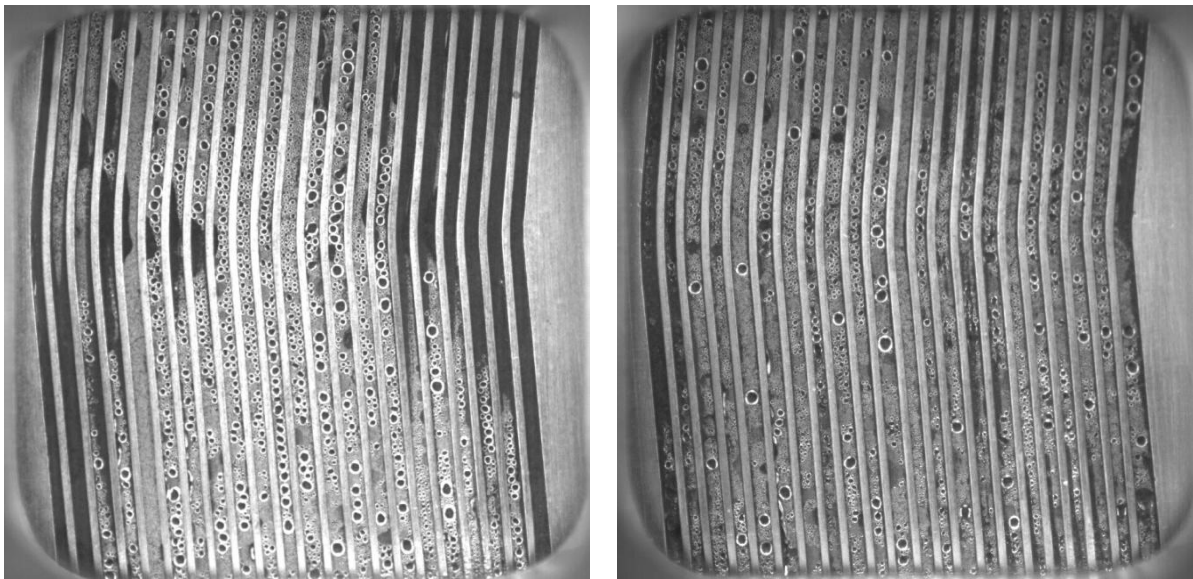
At this stoichiometric ratio, the Freudenberg sample showed an initial increase in the anode channel water at lower current densities due to the significantly increased reactant flow, but at higher current densities the increased flow rates were capable of purging most water from the channels. The Freudenberg cathode maintained similar water levels overall compared to the 1.5/5 condition, and the anode still predominantly maintained slug flow at low to mid current densities. Mist regions developed in the flow fields much sooner as a result elevated gas flow levels of this stoichiometric ratio. The Toray GDL exhibited less liquid water in the channels due to the increased flow rates. Sample flow field images are shown in Figures 5.10 and 5.11.



(a)

(b)

Figure 5.10 - Comparison of cathode window #1 for (a) Freudenberg and (b) Toray at stoichiometric ratio (an/ca) 3/8 and current density 100 mA/cm².



(a)

(b)

Figure 5.11 - Comparison of cathode window #2 for (a) Freudenberg and (b) Toray at stoichiometric ratio (an/ca) 3/8 and current density 100 mA/cm².

5.3. Automatic Detection of Static and Dynamic Liquid Water

The video processing algorithm developed in this work as described in Section 4.4. was used to automatically detect liquid water present in the flow field channels as recorded using the dual-visualization setup. A major advantage of this technique compared to manual observation and selection of water regions is its ability to capture dynamic liquid water in the channels in addition to static water. Figures 5.12 – 5.14 show examples of processed frames

with liquid water detection, while Figure 5.15 (a)-(d) shows a sequence capturing dynamic movement of a cathode slug.

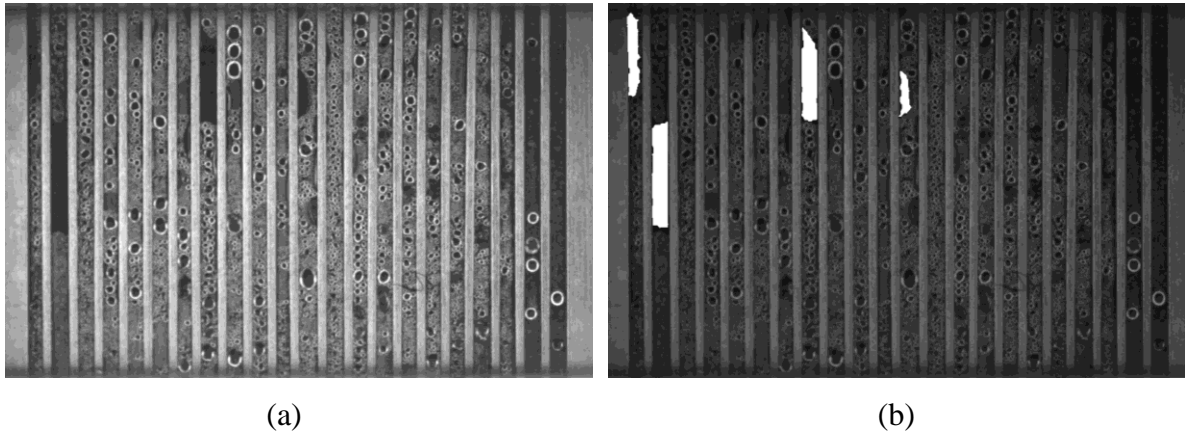


Figure 5.12 - Liquid water detection for cathode window #1 with Freudenberg GDL at stoichiometric ratio (an/ca) 1.5/5 and current density 50 mA/cm²: (a) pre-processed image, (b) processed image.

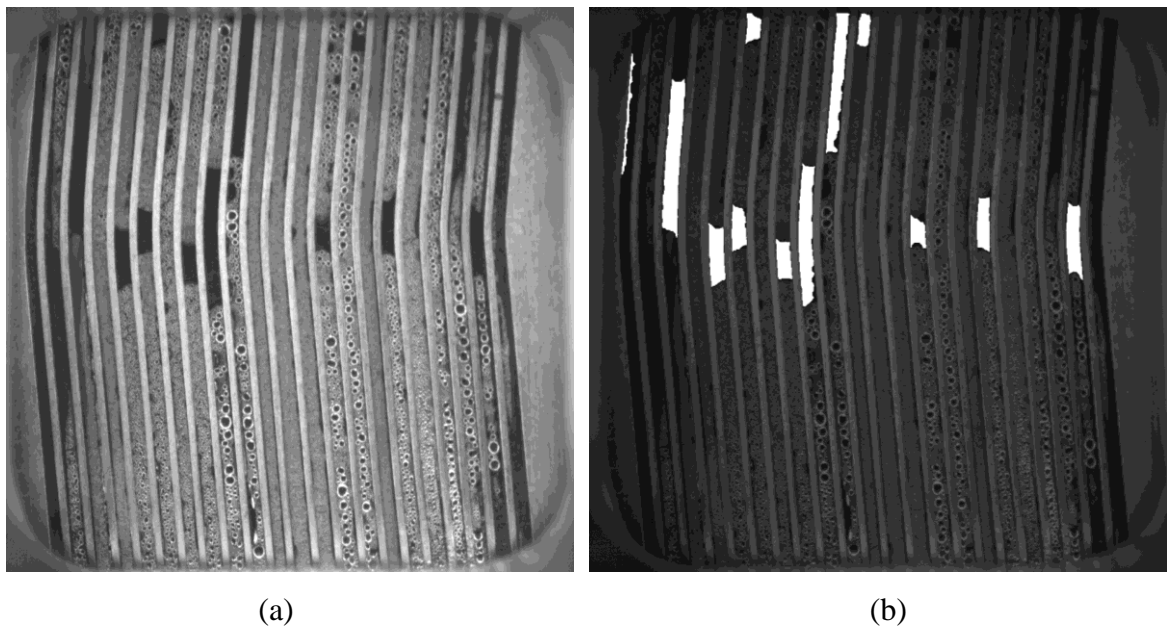
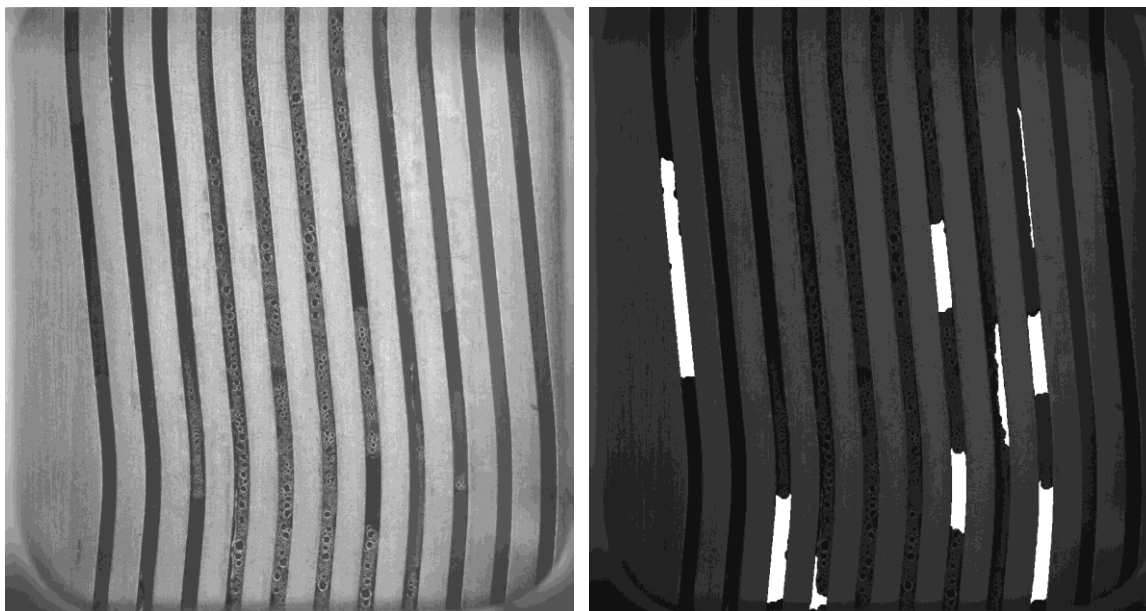


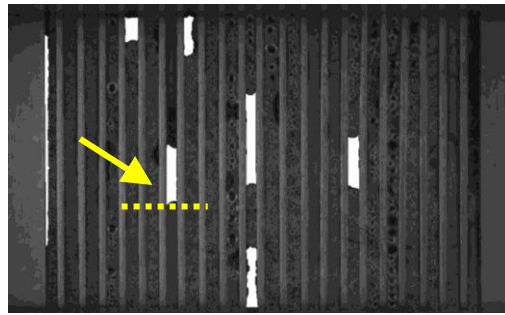
Figure 5.13 - Liquid water detection for cathode window #2 with Freudenberg GDL at stoichiometric ratio (an/ca) 1.5/2.5 and current density 100 mA/cm²: (a) pre-processed image, (b) processed image.



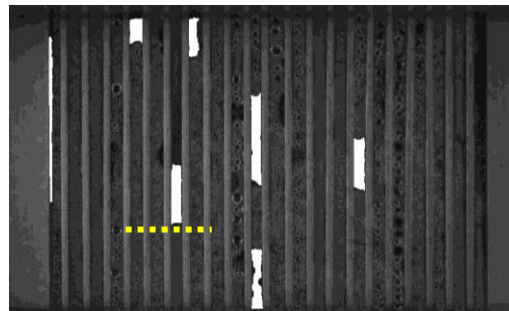
(a)

(b)

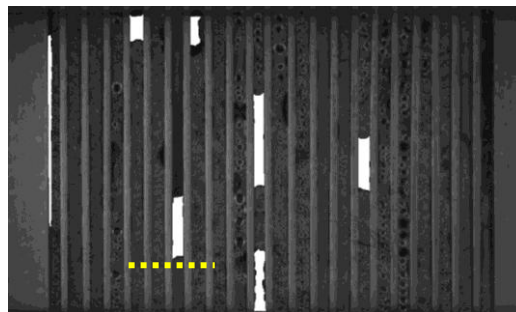
Figure 5.14 - Liquid water detection for anode window #2 with Freudenberg GDL at stoichiometric ratio (an/ca) 1.5/2.5 and current density 100 mA/cm²: (a) pre-processed image, (b) processed image.



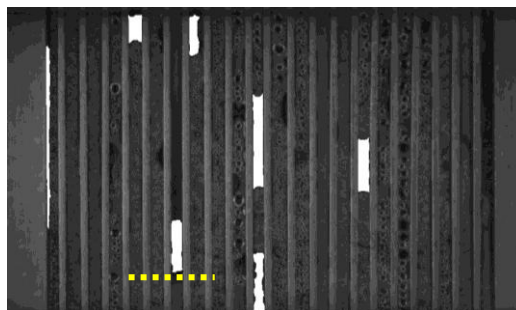
(a) 0 sec



(b) 0.38 sec



(c) 0.70 sec



(d) 1 sec

Figure 5.15 - Sequence showing capture and detection of dynamic slug movement in cathode channel #7 of window #1 with Freudenberg GDL at stoichiometric ratio (a_n/c_a) 1.5/2.5 and current density 150 mA/cm^2 . The dotted yellow line placed at the bottom of the slug highlights its travel.

5.4. Water Coverage Ratio

One of the primary objectives of this work was to develop a technique to automatically generate quantitative data pertaining to the amount of liquid water in the flow field channels using optical visualization. To achieve this, a video processing algorithm was developed and implemented as described in Section 4.4. The algorithm generated quantitative data from the test videos recorded using the dual-visualization setup. The water coverage ratio parameter was introduced to quantify the amount of liquid water present in the channels, and is defined as the total area of liquid water present in the flow field channels divided by the total projected channel area. This parameter was calculated for both GDL samples at each test condition and stoichiometric ratio. As described in Section 3.3.4., multiple videos were typically recorded for each window at a given operating condition. The average water coverage area (in pixels) was calculated for each video, and then averaged for each window. The sum of the averages for all windows was taken to represent the average total flow field water coverage at each condition, which was divided by the total channel area (in pixels) to yield the water coverage ratio which is presented in this section.

5.4.1. Stoichiometric Ratio 1.5/2.5

This stoichiometric ratio showed the highest presence of liquid water in the channels for each GDL sample, especially on the anode side of the cell. A comparison of the water coverage ratio for the anode and cathode of each GDL sample is shown in Figure 5.16.

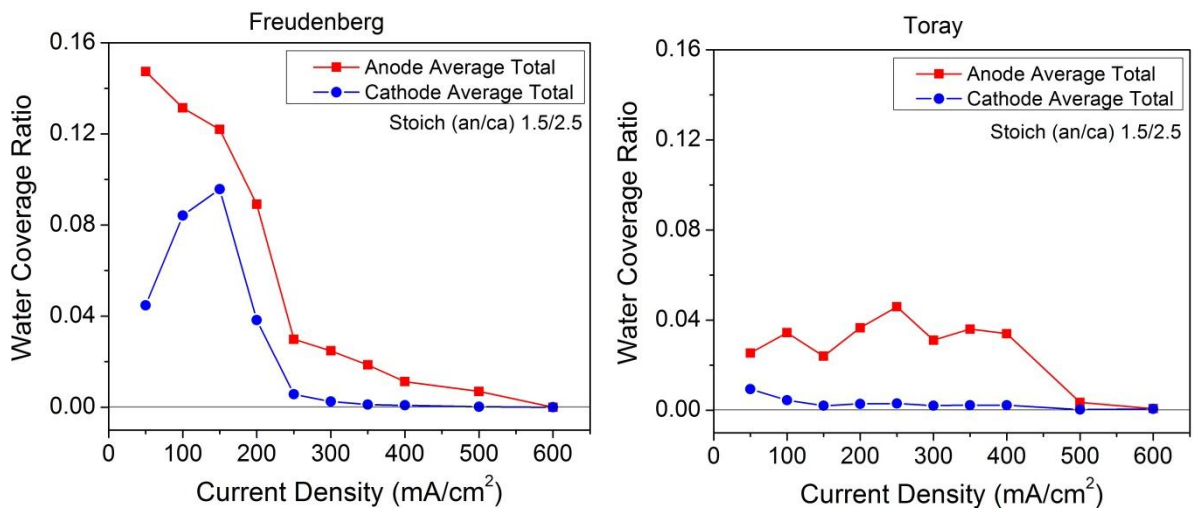


Figure 5.16 - Comparison of anode and cathode water coverage ratio for Freudenberg (left) and Toray (right) GDL samples, at stoichiometric ratio (an/ca) 1.5/2.5.

For the Freudenberg sample, the anode water coverage was found to be significantly higher than the cathode at lower current densities, with a maximum water coverage ratio of 0.147 at 50 mA/cm². The peak cathode water condition occurred at 150 mA/cm² with a water coverage ratio of 0.096. Both flow fields demonstrated higher water coverage at low to mid current densities, and the coverage tapered off as higher current densities were approached due to the increased gas flow rate and cell heat effects. The Toray GDL sample did not exhibit as much water in the channels as the Freudenberg GDL. The anode flow field maintained a water coverage ratio of 0.025 to 0.046 in the low to mid current density range, which tapered off at higher current densities. The cathode water coverage ratio was relatively constant and did not exceed 0.009.

5.4.2. Stoichiometric Ratio 1.5/5

Figure 5.17 shows a comparison of the water coverage ratio for the anode and cathode of each GDL sample at a stoichiometric ratio of 1.5/5.

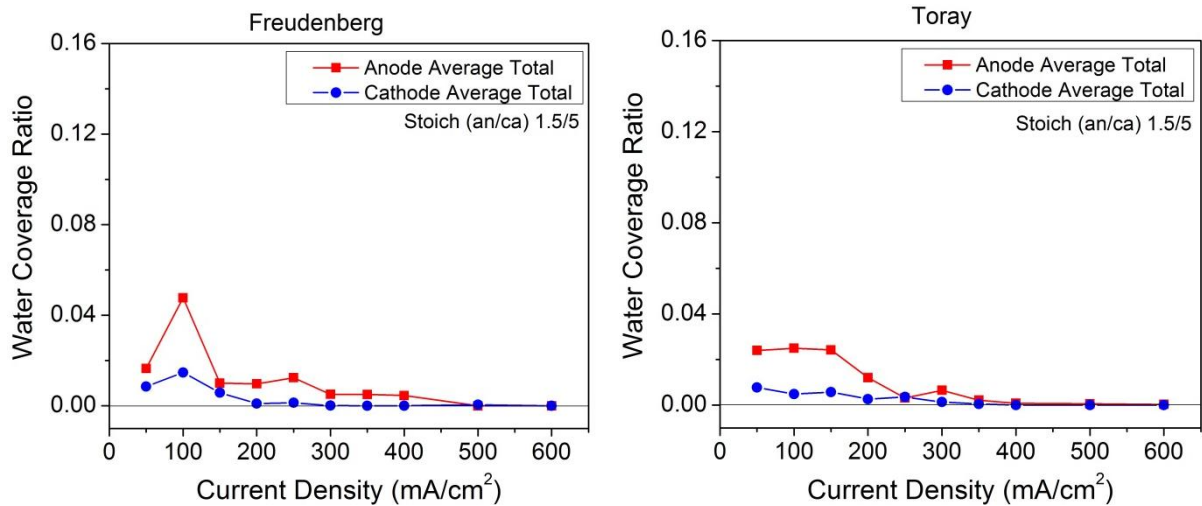


Figure 5.17 - Comparison of anode and cathode water coverage ratio for Freudenberg (left) and Toray (right) GDL samples, at stoichiometric ratio (an/ca) 1.5/5.

The anode and cathode water coverage ratios at this stoichiometric ratio for both GDL samples were considerably less than the 1.5/2.5 condition. The maximum anode coverage for Freudenberg decreased from 0.147 at 50 mA/cm² to 0.048 at 100 mA/cm². The peak cathode water coverage decreased from 0.096 at 150 mA/cm² to 0.015 at 100 mA/cm². The water content for both flow fields exhibited the same trend as the lower stoichiometric ratio, with

higher water content occurring at low current density and tapering off as the current was increased. Aside from the increased water coverage at low current density for Freudenberg, the two GDL samples demonstrated comparable water coverage at this stoichiometric ratio. The anode water coverage ratio for the Toray GDL was decreased overall with peak water coverage of 0.025, and also tapered off at a much lower current density compared to the 1.5/2.5 stoichiometric ratio. The Toray cathode did not demonstrate any significant changes in water coverage overall.

5.4.3. Stoichiometric Ratio 3/8

A comparison of the water coverage ratio for the anode and cathode of each GDL at a stoichiometric ratio of 3/8 is shown in Figure 5.18.

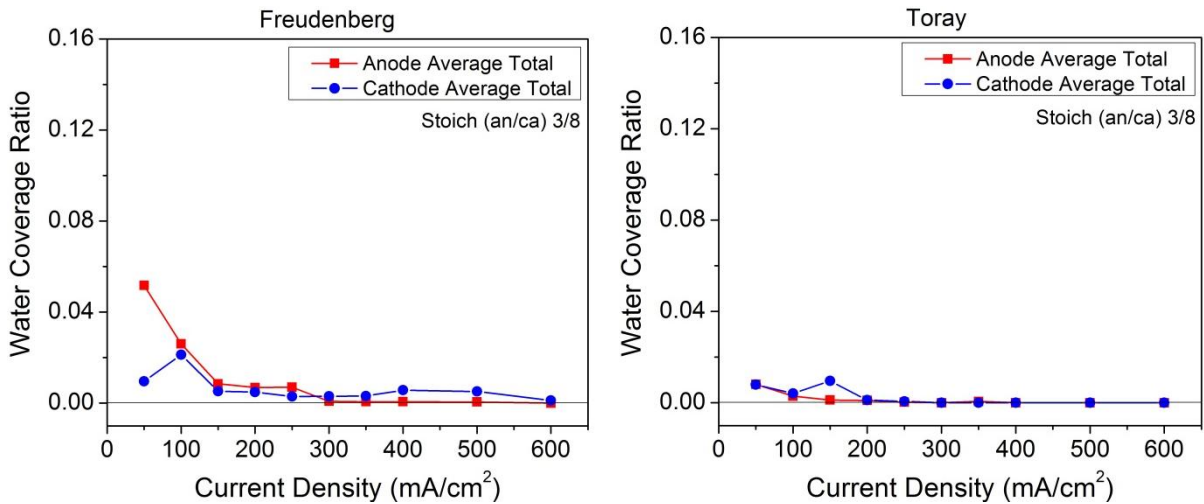


Figure 5.18 - Comparison of anode and cathode water coverage ratio for Freudenberg (left) and Toray (right) GDL samples, at stoichiometric ratio (an/ca) 3/8.

Under these conditions, the Freudenberg anode demonstrated an initial increase in water content at low current density due to the increased reactant flow, with a water coverage ratio as high as 0.052 at 50 mA/cm². This effect was soon countered by the ability of the higher reactant flow rates to remove liquid water from the channels, and the coverage ratio decreased for successive current densities. The cathode water coverage ratio did not show significant differences in trend or quantity compared to the previous stoichiometric ratio. The Toray GDL exhibited almost no water in the anode flow field, with a maximum coverage ratio of 0.008 at the lowest current density, and no flow field water present starting

at 250 mA/cm². The cathode water content did not differentiate substantially from the 1.5/5 stoichiometric ratio, but was slightly less at each current density, and no flow field water present starting at 300 mA/cm².

5.4.4. Tabulated Water Coverage Ratio Results

The water coverage results for each operating condition and GDL sample that were obtained using the video processing algorithm are presented in Tables 5.1 and 5.2.

Table 5.1 - Freudenberg GDL water coverage ratio results.

Current Density (mA/cm ²)	Stoichiometric Ratio (an/ca)					
	1.5/2.5		1.5/5		3/8	
	Anode	Cathode	Anode	Cathode	Anode	Cathode
50	0.147	0.045	0.016	0.009	0.052	0.010
100	0.131	0.084	0.048	0.015	0.026	0.021
150	0.122	0.096	0.010	0.006	0.008	0.005
200	0.089	0.038	0.010	0.001	0.007	0.005
250	0.030	0.006	0.012	0.001	0.007	0.003
300	0.025	0.003	0.005	0.000	0.001	0.003
350	0.019	0.001	0.005	0.000	0.001	0.003
400	0.011	0.001	0.005	0.000	0.001	0.006
500	0.007	0.000	0.000	0.000	0.001	0.005
600	0.000	0.000	0.000	0.000	0.000	0.001

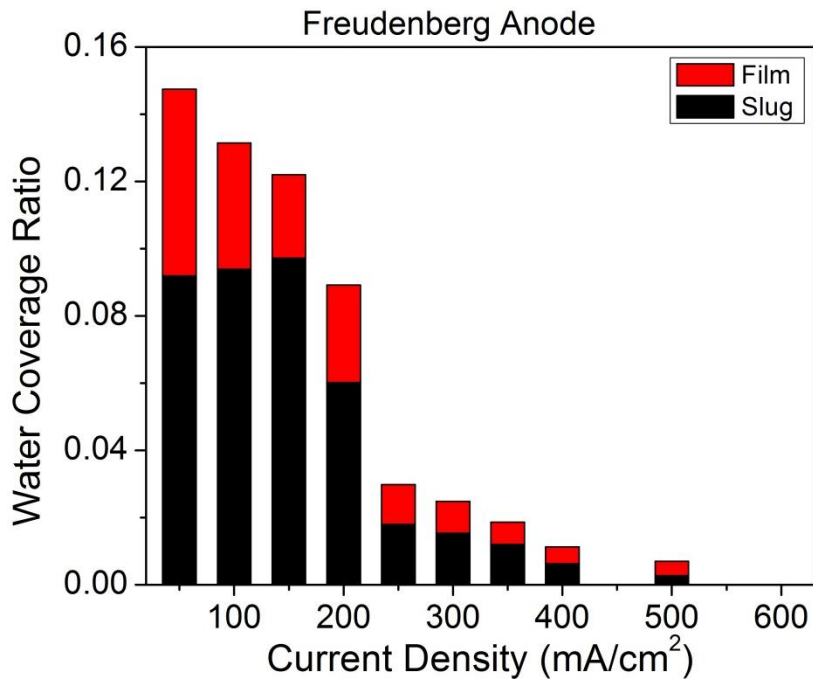
Table 5.2 - Toray GDL water coverage ratio results.

Current Density (mA/cm ²)	Stoichiometric Ratio (an/ca)					
	1.5/2.5		1.5/5		3/8	
	Anode	Cathode	Anode	Cathode	Anode	Cathode
50	0.025	0.009	0.024	0.008	0.008	0.008
100	0.034	0.004	0.025	0.005	0.003	0.004
150	0.024	0.002	0.024	0.006	0.001	0.010
200	0.037	0.003	0.012	0.003	0.001	0.001
250	0.046	0.003	0.003	0.004	0.000	0.001
300	0.031	0.002	0.007	0.001	0.000	0.000
350	0.036	0.002	0.002	0.001	0.000	0.000
400	0.034	0.002	0.001	0.000	0.000	0.000
500	0.003	0.000	0.001	0.000	0.000	0.000
600	0.001	0.000	0.000	0.000	0.000	0.000

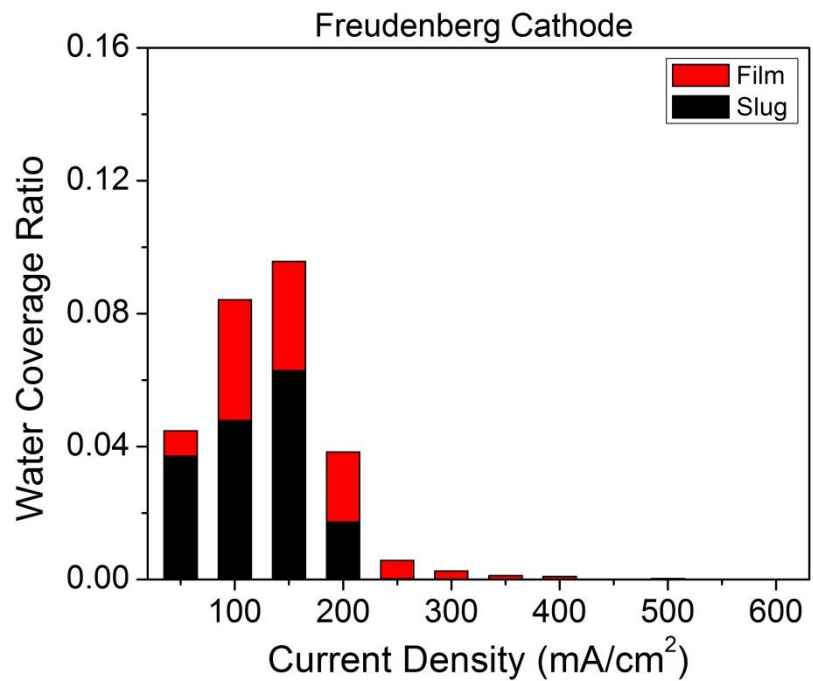
5.5. Flow Structure Differentiation and Water Distribution

In addition to quantifying the liquid water, determining the type of flow structures present helps to further characterize two-phase flow in the gas channels. A video processing algorithm was developed in order to analyze the liquid water detected in the flow field channels and classify its flow structure, as described in Section 4.6. The resulting information was used to calculate the average distribution of detected liquid water among the different flow structures (film flow and slug flow). This was calculated for the anode and cathode of both GDL samples at a stoichiometric ratio of 1.5/2.5. The average number of slugs and films was calculated for each video taken at a particular current density and window. These results were averaged for each window, and the sum of the average flow structure counts (i.e. the number of slugs and films) was taken for all windows, representing the total average counts for the entire flow field at each operating condition. These counts were then used to calculate the average water distribution from the water coverage results.

Figure 5.19 (a) and (b) show the average water distribution among the different flow structures for the anode and cathode of the Freudenberg GDL sample at each current density. A comparison of the two flow fields clearly shows tendency of slug flow to account for the majority of liquid water on the anode side for all current densities prior to 500 mA/cm^2 , whereas the cathode water distribution majority transitions from slug to film flow at 200 mA/cm^2 . Figure 5.20 (a) and (b) show the average water distribution among the different flow structures for the anode and cathode of the Toray GDL sample at each current density.

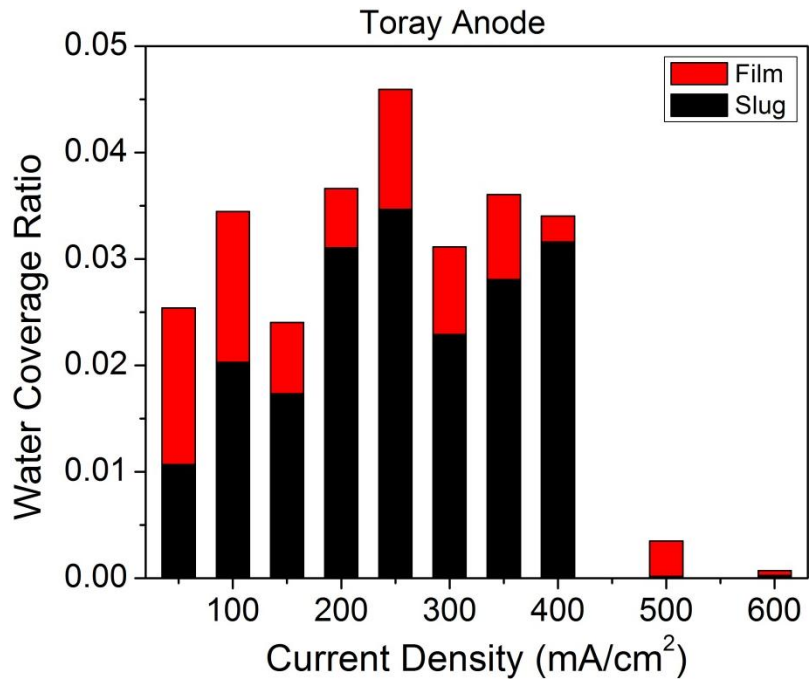


(a)

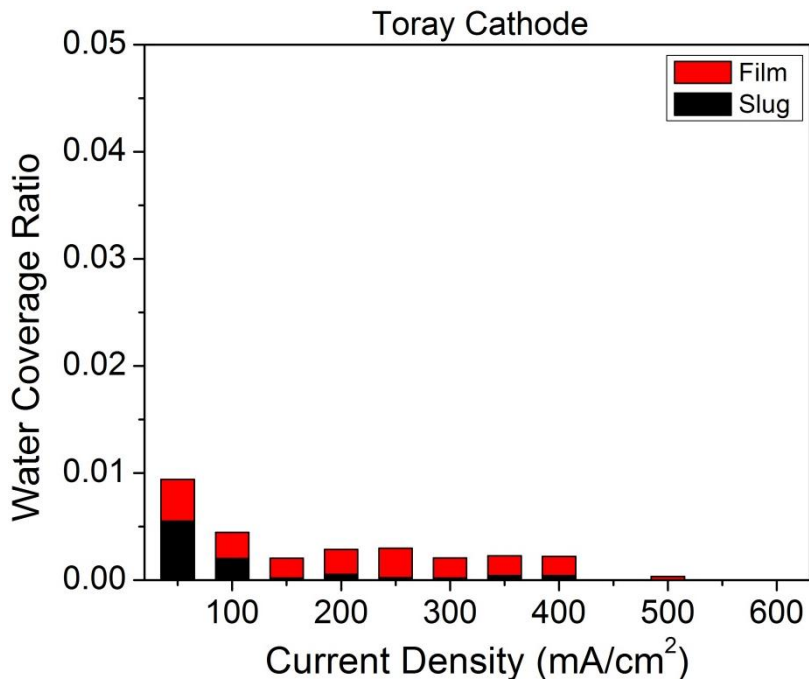


(b)

Figure 5.19 – Distribution of liquid water among flow structures at stoichiometric ratio 1.5/2.5 for (a) Freudenberg anode flow field and (b) Freudenberg cathode flow field.



(a)



(b)

Figure 5.20 – Distribution of liquid water among flow structures at stoichiometric ratio 1.5/2.5 for (a) Toray anode flow field and (b) Toray cathode flow field. Note different scaling for water coverage ratio compared to Freudenberg GDL plots.

As was seen with the Freudenberg sample, the Toray anode water is also predominantly attributed to slug flow. Aside from the lowest current density, the majority of Toray cathode water is a result of film flow.

5.5.1. Tabulated Water Distribution Results

Tabulated results showing both the average water distribution percentages and the average number of water objects accounting for the percentages at each operating condition for the two GDL samples are presented in Tables 5.3 and 5.4. The total number of water objects present for both the anode and the cathode flow fields was shown to be significantly less for the Toray GDL compared to Freudenberg GDL.

Table 5.3 – Freudenberg GDL water distribution results.

Freudenberg GDL (Stoich 1.5/2.5)										
Current Density (mA/cm ²)	Anode					Cathode				
	Water Coverage Ratio	% Slug	# Slug Objects	% Film	# Film Objects	Water Coverage Ratio	% Slug	# Slug Objects	% Film	# Film Objects
50	0.147	62	20.64	38	31.91	0.045	83	22.45	17	21.19
100	0.131	71	22.92	29	19.95	0.084	57	31.56	43	45.91
150	0.122	80	23.38	20	13.57	0.096	66	33.63	34	35.08
200	0.089	68	17.64	32	15.06	0.038	45	15.01	55	22.22
250	0.030	60	3.18	40	6.05	0.006	3	0.26	97	7.14
300	0.025	62	2.66	38	6.32	0.003	3	0.09	97	3.92
350	0.019	64	2.34	36	4.52	0.001	8	0.16	92	1.90
400	0.011	56	1.32	44	2.60	0.001	2	0.04	98	1.46
500	0.007	38	1.17	62	2.38	0.000	0	0.00	0	0.00
600	0.000	0	0.00	0	0.00	0.000	0	0.00	0	0.00

Table 5.4 – Toray GDL water distribution results.

Toray GDL (Stoich 1.5/2.5)										
Current Density (mA/cm ²)	Anode					Cathode				
	Water Coverage Ratio	% Slug	# Slug Objects	% Film	# Film Objects	Water Coverage Ratio	% Slug	# Slug Objects	% Film	# Film Objects
50	0.025	42	4.54	58	12.47	0.009	59	3.79	41	5.79
100	0.034	59	7.13	41	8.82	0.004	45	2.51	55	5.30
150	0.024	72	5.01	28	5.88	0.002	10	0.45	90	4.72
200	0.037	85	7.00	15	5.07	0.003	19	0.95	81	5.72
250	0.046	75	7.33	25	9.51	0.003	7	0.47	93	7.06
300	0.031	74	8.84	26	7.38	0.002	9	0.40	91	5.04
350	0.036	78	4.68	22	6.57	0.002	19	0.96	81	4.20
400	0.034	93	5.76	7	2.20	0.002	19	0.70	81	4.35
500	0.003	5	0.16	95	3.41	0.000	0	0.00	0	0.00
600	0.001	37	0.19	63	0.39	0.000	0	0.00	0	0.00

5.6. Summary of Experimental Results

Experiments were conducted on the transparent fuel cell equipped with a dual-visualization feature for simultaneous anode and cathode observation. Recorded test videos were processed in a newly developed algorithm to identify water coverage in the flow field channels. The algorithm was able to successfully capture and represent the visual observations of flow field water described in with quantitative metrics. The water coverage ratio parameter was introduced to quantify the presence of water in the gas channels. Through both visual observation and quantitative metrics derived from the video processing algorithm, the Freudenberg GDL consistently demonstrated a higher water coverage ratio in the flow field gas channels. The water residing in the channels is more readily purged from the cell at higher gas flow rates (current densities), and the cell can become susceptible to an accelerated dehydration (which for this particular cell was exacerbated by the heating effects caused by the transparent windows). This was evident from the spike in HFR for the Freudenberg GDL at high current density, indicating increased ionic transport resistance within the cell, and the subsequent decrease in cell performance. The Toray GDL maintained comparable performance and HFR to the Freudenberg GDL at low to mid current densities, and exhibited better performance and lower HFR at high current density, indicating an increased membrane hydration state. Along with its overall lower water coverage ratio, this indicates a propensity for higher water retention within the MEA for Toray GDL.

6. Conclusions

A technique was developed to obtain quantitative metrics for liquid water in the gas channels of a transparent PEM fuel cell using digital video processing. The small scale fuel cell geometry was designed to be representative of actual full scale automotive fuel cell hardware. A dual-visualization setup was implemented in order to simultaneously observe the anode and cathode flow fields during cell operation. A video processing algorithm was developed to automatically detect and quantify the liquid water present in the flow fields as the water coverage ratio, and also determine the distribution of water among the different two-phase flow structures present. Freudenberg and Toray GDL samples were tested at 35°C with fully humidified inlet gases for a range of current densities at stoichiometric ratios (an/ca) of 1.5/2.5, 1.5/5, and 3/8.

Based on the presented study, the following conclusions are drawn:

- The performance and HFR measurements for the Freudenberg and Toray GDLs were found to be comparable for low to mid current densities, with Toray performance exceeding Freudenberg at high current density, while maintaining an increased membrane hydration state. This was observed for all stoichiometric ratios tested.
- A parameter called the water coverage ratio, defined as the total liquid water present in the flow field channels divided by the total channel area, was introduced to quantify the presence of liquid water in the channels. The Freudenberg GDL consistently demonstrated a higher water coverage ratio than the Toray GDL. The anode water coverage ratio was found to exceed the cathode for both GDL samples at most operating conditions.
- The water distribution results for a stoichiometric ratio of 1.5/2.5 indicated that for Freudenberg GDL, slug flow was dominant on the anode for both GDL samples except at high current density, when film flow became dominant. The majority of water on Freudenberg cathode was attributed to slug flow at lower current densities, and film flow for mid to high current densities. Film flow was dominant for the Toray cathode except at the lowest current density. Overall the

number of water objects detected for the Freudenberg GDL was much higher than that of the Toray GDL for both flow fields.

- The tendency for more liquid water to be present in the channels of the Freudenberg cell facilitated water removal at high flow rates (current densities), contributing to membrane dehydration and reduced performance. This was amplified by the heating effects of the cell's transparent windows. The Toray GDL maintained higher performance and lower HFR measurements at high current density, indicating the likelihood of greater water retention within the MEA.

The automatic detection of static and dynamic liquid water in the fuel cell flow fields, combined with flow structure differentiation and water distribution, provided a comprehensive quantitative characterization of two-phase flow present in the gas channels. This technique can be used to generate data for model validation purposes, for the optimization of materials and operating conditions for water management, as well as the development of appropriate purge sequences. The dual-visualization system can be used to elucidate the effect of water transport across the membrane on anode and cathode flow field dynamics.

7. Recommendations for Future Work

The video processing algorithms developed in this work could be expanded to include additional analysis of the dynamic liquid water transport, e.g. the frequency, residence time, and velocity of liquid water objects in the channels. Additionally, the implementation of a less insulating window material, such as quartz, would be helpful in mitigating heating effects and the subsequent premature dehydration of the cell. A systematic study of GDL materials could be performed using this technique to further elucidate the effects of microstructure, thickness, porosity, PTFE content, and MPL coating on two-phase flow.

8. References

- [1] Kandlikar, S., 2008, "Microscale and Macroscale Aspects of Water Management Challenges in PEM Fuel Cells," *Heat Transfer Engineering*, 29(7), pp. 575-587.
- [2] Kandlikar, S. G., and Lu, Z., 2009, "Fundamental Research Needs in Combined Water and Thermal Management within a Proton Exchange Membrane Fuel Cell Stack under Normal and Cold-Start Conditions," *Journal of Fuel Cell Science and Technology*, 6(4), pp. 044001-13.
- [3] Anderson, R., Zhang, L., Ding, Y., Blanco, M., Bi, X., and Wilkinson, D. P., 2010, "A Critical Review of Two-Phase Flow in Gas Flow Channels of Proton Exchange Membrane Fuel Cells," *Journal of Power Sources*, 195(15), pp. 4531-4553.
- [4] Li, H., Tang, Y., Wang, Z., Shi, Z., Wu, S., Song, D., Zhang, J., Fatih, K., Zhang, J., Wang, H., Liu, Z., Abouatallah, R., and Mazza, A., 2008, "A Review of Water Flooding Issues in the Proton Exchange Membrane Fuel Cell," *Journal of Power Sources*, 178(1), pp. 103-117.
- [5] Owejan, J. P., Gagliardo, J. J., Sergi, J. M., Kandlikar, S. G., and Trabold, T. A., 2009, "Water Management Studies in PEM Fuel Cells, Part I: Fuel Cell Design and In Situ Water Distributions," *International Journal of Hydrogen Energy*, 34(8), pp. 3436-3444.
- [6] Spornjak, D., Advani, S. G., and Prasad, A. K., 2009, "Simultaneous Neutron and Optical Imaging in PEM Fuel Cells," *Journal of The Electrochemical Society*, 156(1), pp. B109-B117.
- [7] Zhang, F. Y., Yang, X. G., and Wang, C. Y., 2006, "Liquid Water Removal from a Polymer Electrolyte Fuel Cell," *Journal of The Electrochemical Society*, 153(2), pp. A225-A232.
- [8] Liu, X., Guo, H., Ye, F., and Ma, C. F., 2008, "Flow Dynamic Characteristics in Flow Field of Proton Exchange Membrane Fuel Cells," *International Journal of Hydrogen Energy*, 33(3), pp. 1040-1051.
- [9] Ge, S., and Wang, C.-Y., 2007, "Liquid Water Formation and Transport in the PEFC Anode," *Journal of The Electrochemical Society*, 154(10), pp. B998-B1005.
- [10] O'rourke, J., Ramani, M., and Arcaç, M., 2009, "In Situ Detection of Anode Flooding of a PEM Fuel Cell," *International Journal of Hydrogen Energy*, 34(16), pp. 6765-6770.
- [11] Spornjak, D., Prasad, A. K., and Advani, S. G., 2007, "Experimental Investigation of Liquid Water Formation and Transport in a Transparent Single-Serpentine PEM Fuel Cell," *Journal of Power Sources*, 170(2), pp. 334-344.

- [12] Owejan, J. P., Trabold, T. A., Jacobson, D. L., Arif, M., and Kandlikar, S. G., 2007, "Effects of Flow Field and Diffusion Layer Properties on Water Accumulation in a PEM Fuel Cell," *International Journal of Hydrogen Energy*, 32(17), pp. 4489-4502.
- [13] Hussaini, I. S., and Wang, C.-Y., 2009, "Visualization and Quantification of Cathode Channel Flooding in PEM Fuel Cells," *Journal of Power Sources*, 187(2), pp. 444-451.
- [14] Ma, H. P., Zhang, H. M., Hu, J., Cai, Y. H., and Yi, B. L., 2006, "Diagnostic Tool to Detect Liquid Water Removal in the Cathode Channels of Proton Exchange Membrane Fuel Cells," *Journal of Power Sources*, 162(1), pp. 469-473.
- [15] Liu, X., Guo, H., Ye, F., and Ma, C. F., 2007, "Water Flooding and Pressure Drop Characteristics in Flow Channels of Proton Exchange Membrane Fuel Cells," *Electrochimica Acta*, 52(11), pp. 3607-3614.
- [16] Lu, Z., Kandlikar, S. G., Rath, C., Grimm, M., Domigan, W., White, A. D., Hardbarger, M., Owejan, J. P., and Trabold, T. A., 2009, "Water Management Studies in PEM Fuel Cells, Part II: Ex Situ Investigation of Flow Maldistribution, Pressure Drop and Two-Phase Flow Pattern in Gas Channels," *International Journal of Hydrogen Energy*, 34(8), pp. 3445-3456.
- [17] Hakenjos, A., Muentner, H., Wittstadt, U., and Hebling, C., 2004, "A PEM Fuel Cell for Combined Measurement of Current and Temperature Distribution, and Flow Field Flooding," *Journal of Power Sources*, 131(1-2), pp. 213-216.
- [18] Liu, X., Guo, H., and Ma, C., 2006, "Water Flooding and Two-Phase Flow in Cathode Channels of Proton Exchange Membrane Fuel Cells," *Journal of Power Sources*, 156(2), pp. 267-280.
- [19] Owejan, J. P., Trabold, T. A., Jacobson, D. L., Baker, D. R., Hussey, D. S., and Arif, M., 2006, "In Situ Investigation of Water Transport in an Operating PEM Fuel Cell Using Neutron Radiography: Part 2 - Transient Water Accumulation in an Interdigitated Cathode Flow Field," *International Journal of Heat and Mass Transfer*, 49(25-26), pp. 4721-4731.
- [20] Park, J., Li, X., Tran, D., Abdel-Baset, T., Hussey, D. S., Jacobson, D. L., and Arif, M., 2008, "Neutron Imaging Investigation of Liquid Water Distribution in and the Performance of a PEM Fuel Cell," *International Journal of Hydrogen Energy*, 33(13), pp. 3373-3384.
- [21] Sugiura, K., Nakata, M., Yodo, T., Nishiguchi, Y., Yamauchi, M., and Itoh, Y., 2005, "Evaluation of a Cathode Gas Channel with a Water Absorption Layer/Waste Channel in a PEFC by Using Visualization Technique," *Journal of Power Sources*, 145(2), pp. 526-533.
- [22] Trabold, T. A., Owejan, J. P., Jacobson, D. L., Arif, M., and Huffman, P. R., 2006, "In Situ Investigation of Water Transport in an Operating PEM Fuel Cell Using Neutron Radiography: Part 1 - Experimental Method and Serpentine Flow Field Results," *International Journal of Heat and Mass Transfer*, 49(25-26), pp. 4712-4720.

- [23] Tüber, K., Póczy, D., and Hebling, C., 2003, "Visualization of Water Buildup in the Cathode of a Transparent PEM Fuel Cell," *Journal of Power Sources*, 124(2), pp. 403-414.
- [24] Weng, F.-B., Su, A., Hsu, C.-Y., and Lee, C.-Y., 2006, "Study of Water-Flooding Behaviour in Cathode Channel of a Transparent Proton-Exchange Membrane Fuel Cell," *Journal of Power Sources*, 157(2), pp. 674-680.
- [25] Weng, F.-B., Su, A., and Hsu, C.-Y., 2007, "The Study of the Effect of Gas Stoichiometric Flow Rate on the Channel Flooding and Performance in a Transparent Fuel Cell," *International Journal of Hydrogen Energy*, 32(6), pp. 666-676.
- [26] Yang, X. G., Zhang, F. Y., Lubawy, A. L., and Wang, C. Y., 2004, "Visualization of Liquid Water Transport in a PEFC," *Electrochemical and Solid-State Letters*, 7(11), pp. A408-A411.
- [27] Bazylak, A., 2009, "Liquid Water Visualization in PEM Fuel Cells: A Review," *International Journal of Hydrogen Energy*, 34(9), pp. 3845-3857.
- [28] St-Pierre, J., 2007, "PEMFC In Situ Liquid-Water-Content Monitoring Status," *Journal of The Electrochemical Society*, 154(7), pp. B724-B731.
- [29] Yamauchi, M., Sugiura, K., Yamauchi, T., Taniguchi, T., and Itoh, Y., 2009, "Proposal for an Optimum Water Management Method Using Two-Pole Simultaneous Measurement," *Journal of Power Sources*, 193(1), pp. 1-8.
- [30] Spornjak, D., Prasad, A. K., and Advani, S. G., 2010, "In Situ Comparison of Water Content and Dynamics in Parallel, Single-Serpentine, and Interdigitated Flow Fields of Polymer Electrolyte Membrane Fuel Cells," *Journal of Power Sources*, 195(11), pp. 3553-3568.
- [31] Sergi, J. M., Lu, Z., and Kandlikar, S. G., 2009, "In Situ Characterization of Two-Phase Flow in the Cathode Channels of an Operating PEM Fuel Cell with Visual Access," Pohang, South Korea.
- [32] Gonzalez, R. C., and Woods, R. E., 2008, *Digital Image Processing*, Pearson Education, Inc., Upper Saddle River, NJ.
- [33] Gonzalez, R. C., Woods, R. E., and Eddins, S. L., 2004, *Digital Image Processing Using Matlab*, Pearson Education, Inc., Upper Saddle River, NJ.
- [34] Soille, P., 2004, *Morphological Image Analysis*, Springer, Berlin.
- [35] Dougherty, E. R., and Lotufo, R. A., 2003, *Hands-on Morphological Image Processing*, SPIE, Bellingham, Washington.

9. Appendices

9.1. Appendix A: Water Detection and Quantification Algorithm (MATLAB)

```
function vidprocess_annotated(file_directory)
tic;
videos=dir(strcat(file_directory, '\*.avi'));
fileNames={videos.name}' %lists avi file names in directory
nVideos=length(fileNames); %number of avi files listed
maskfile=dir(strcat(file_directory, '\*_mask.tif'));
maskname={maskfile.name}'%lists mask file name in directory
maskname=maskfile.name;

for i=1:nVideos-1
    wetvid=fileNames{i};
    dryvid=fileNames{nVideos};
    %%Image Processing
    wet=mmreader(wetvid); %reading in the input videos
    dry=mmreader(dryvid);
    nframes_wet=wet.NumberOfFrames;%defining number of frames
    nframes_dry=dry.NumberOfFrames;

    refframe=read(dry,1); %reading the first frame of the ref video
    q=double(refframe(:,:,1)); %convert to single plane, double

    %loop to average reference (dry) video to single frame
    for n=2:nframes_dry
        k=read(dry,n);
        k=double(k(:,:,1));
        q=q+k;
    end
    avgframe=q./nframes_dry;
    avgframe=avgframe./mean(avgframe(:));
    avgframe=avgframe./255; %scaling from double

    %%Mask File%%
    mask=imread(maskname);
    mask=logical(mask);
    mask=im2double(mask(:,:,1));
    num_ch_pix=length(find(mask));

    %%setup for new processed video file being created in loop
    F=findstr('.avi',wetvid);
    newfilename=wetvid(1:F-1);

    mov=avifile(strcat(file_directory, '\', newfilename, '_proc', '.avi'), 'colormap', gray(256), 'fps', 60, 'compression', 'none');

    num_wet_pix=zeros(1,nframes_wet);

    %loop to subtract reference frame from each video frame, perform
    %morphological processing, and stitch processed frames together into
new
    %video file
```

```

for n=1:nframes_wet
    vid=read(wet,n);
    vid=double(vid(:,:,1));
    vid=vid./mean(vid(:));
    vid=vid./255; %scaling
    diff=imabsdiff(vid,avgframe);%absolute difference of video frame
and average frame from reference video
    diff=diff.*mask;
    maxpixelval=max(diff(:));%maximum pixel value in difference frame
    diff=diff./maxpixelval; %normalizing frame by max pixel value
    thresh=diff>(lowerthreshval/255)&diff<(upperthreshval/255);
%threshold - values as determined per batch case
    %%morphological processing
    fill=imfill(thresh,'holes');
    open=bwareaopen(fill,areaopen,400,4);
    bridge=bwmorph(open,'bridge');
    fill=imfill(bridge,'holes');
    se=strel('disk',8);
    close=imclose(fill,se);
    proc_frame=close.*mask;
    %%counting pixels
    numwetpix(n)=length(find(proc_frame)); %number of white (wet)
pixels in processed frame
    %%
    proc_frame=im2uint8(proc_frame); %convert back to unsigned 8-bit
    proc_frame=diff2+im2uint8(50*vid);%add faint unprocessed frame for
spatial context
    %%
    mov=addframe(mov,proc_frame); %add processed frame to new
processed video
end
mov=close(mov);
%%water coverage calculations
avg_wet_pix=mean(num_wet_pix);
pixel_area=0.00111; %area of 1 pixel in mm^2 (for land correlation-
*note this value changes for anode videos)
avg_wet_area=avg_wet_pix*pixel_area; %average area of water in the
channels
ch_area=num_ch_pix*pixel_area; %area of channels
water_coverage_ratio=(avg_wet_pix/num_ch_pix); %ratio of wet area
(based on total channel area)
%%Writing Data To Excel
S=findstr('-10_',wetvid);
P=findstr('_w',wetvid);
shortname=wetvid(S+4:F-1);
filedate=wetvid(5:11);
windownum=wetvid(P:P+2);
datafilename=strcat(filedate>windownum,'_cathode','_data');
header={wetvid};
data={'Single Pixel Area (mm^2)', pixel_area;'Average Number of Wet
Pixels', avg_wet_pix;'Average Wet Area (mm^2)', avg_wet_area; 'Number of
Ch Pixels', num_ch_pix;'Ch Area (mm^2)', ch_area; 'Water Coverage Ratio',
water_coverage_ratio};
warning off MATLAB:xlswrite:AddSheet

xlswrite(strcat(file_directory,'\ ',datafilename,'.xls'),header,shortname);

```

```

xlswrite(strcat(file_directory, '\\', datafilename, '.xls'), data, shortname, 'A3
');
end
toc;

```

9.2. Appendix B: Flow Structure Differentiation Algorithm (MATLAB)

```

function conn_comp(file_directory)
tic;
%%input files from directory
proc_videos=dir(strcat(file_directory, '*_proc.avi'));
proc_fileNames={proc_videos.name}' %lists processed avi file names
nVideos=length(proc_fileNames); %number of avi files listed - should be
same for an and ca
maskfile=dir(strcat(file_directory, '*_mask.tif'));
maskname={maskfile.name}'
maskname=maskfile.name;
mask=imread(maskname);
mask=logical(mask);
mask=im2double(mask(:,:,1));

for i=1:nVideos
    proc_vid=proc_fileNames{i};

    vid=mmreader(proc_vid); %reading in the input videos
    nframes=vid.NumberOfFrames;%defining number of frames - should be same
for an and ca

    F=findstr('.avi',proc_vid);
    newfilename=proc_vid(1:F-1);
    frames_data_matrix=zeros(nframes,9);

    for n=1:nframes

        proc=read(vid,n); %read in proc vid frames
        proc=proc(:,:,1); %convert to single plane
        proc=proc==255; %remove faint reference image
        proc=logical(proc);% turn processed image into logical
        total_water_pix=length(find(proc));

        %%label connected components
        [L,num]=bwlabel(proc); %label connected components, L=labeled
image and num=number conencted components
        num_obj=num; %number of objects in L for video frame n
        combined=imadd(L,mask); %sum of labeled image and mask image:
0=nothing, 1=channel, anything else = channel with water
        label_matrix=zeros(num_obj,3);%preallocate matrix with
rows=#objects and 3 columns: (1) object #, (2) area of object (# of pix),
(3) slug/film (1/0)
        slug_matrix=zeros(num_obj,3);

        %%loop for determining flow strucutre of objects
        for j=1:num_obj;
            obj=combined==j+1; %single object being analyzed

```



```

num_film_pix=total_water_pix-num_slug_pix;
ratio_film_pix=num_film_pix/total_water_pix;
if total_water_pix==0
    ratio_film_pix=0;
end

frames_data_matrix(n,1)=n;
frames_data_matrix(n,2)=total_water_pix;
frames_data_matrix(n,3)=num_obj;
frames_data_matrix(n,4)=num_slugs;
frames_data_matrix(n,5)=num_slug_pix;
frames_data_matrix(n,6)=ratio_slug_pix;
frames_data_matrix(n,7)=num_films;
frames_data_matrix(n,8)=num_film_pix;
frames_data_matrix(n,9)=ratio_film_pix;
end
frames_mean=mean(frames_data_matrix,1);
avg_frames_data=frames_mean(1,2:9);

%%writing data to excel
last_row_num=nframes+7;
last_row_str=num2str(last_row_num);
excel_row=strcat('A',last_row_str);
excel_row_b=strcat('B',last_row_str);
S=findstr('-10_',proc_vid);
P=findstr('_w',proc_vid);
shortname=proc_vid(S+4:F-1);
filedate=proc_vid(5:10);
windownum=proc_vid(P:P+2);
datafilename=strcat(filedate,windownum,'_conn_comp_data');
header={newfilename};
avg_row_name={'Average'};
column_names={'Frame Number','Total Water Pixels','Number of Water
Objects','Number of Slugs','Slug Pixels','Slug Pixel Ratio','Number of
Films','Film Pixels','Film Pixel Ratio'};
%data={frames_data_matrix};
warning off MATLAB:xlswrite:AddSheet

xlswrite(strcat(file_directory,'\ ',datafilename,'.xls'),header,shortname);

xlswrite(strcat(file_directory,'\ ',datafilename,'.xls'),column_names,short
name,'A5');

xlswrite(strcat(file_directory,'\ ',datafilename,'.xls'),frames_data_matrix
,shortname,'A6');

xlswrite(strcat(file_directory,'\ ',datafilename,'.xls'),avg_row_name,short
name,excel_row);

xlswrite(strcat(file_directory,'\ ',datafilename,'.xls'),avg_frames_data,sh
ortname,excel_row_b);

end
toc;

```